Journal of Scientific Computing manuscript No.
(will be inserted by the editor)

Low-Dimensional Spatial Embedding Method for Shape Uncertainty Quantification in Acoustic Scattering

Yuval Harness

Received: date / Accepted: date

arXiv:1704.07727v1 [cs.CE] 25 Apr 2017

Abstract This paper introduces a novel boundary integral approach of shape uncertainty quantification for the Helmholtz scattering problem in the framework of the so-called parametric method. The key idea is to form a low-dimensional spatial embedding within the family of uncertain boundary deformations via the Coarea formula. The embedding, essentially, encompasses any irregular behavior of the boundary deformations and facilitates a low-dimensional integration rule capturing the bulk variation of output functionals defined on the boundary. In a second phase a matching parametric grid is imposed. For the ease of presentation the theory is restricted to $2D$ star-shaped obstacles in low-dimensional setting. We employ the null-field reconstruction technique which is capable of handling large shape deformations. Higher spatial and parametric dimensional cases are discussed, though, not extensively explored in the current study.

Keywords Uncertainty Quantification · Shape Uncertainty · Helmholtz · Parametric Method · Low-dimensional Embedding · Coarea Formula

Mathematics Subject Classification (2010) MSC 49Q15 · MSC 65C99 · MSC 65N35 · MSC 65R20 · MSC 65Z05

1 Introduction

Considerable effort has been devoted in recent years to develop robust and efficient computational strategies for the simulation of physical phenomena, that take into account shape uncertainty. Often, the problem is formulated as an elliptic *partial differential equation* (PDE) whose domain boundaries are uncertain. Such problems arise due to imperfections in manufacturing processes, e.g., in nano-optics where the production of nano particles is, often, inaccurate relatively to nano-scale electromagnetic wave lengths [2]. Other examples arise in the context of

Y. Harness
Inria Bordeaux
Tel.: +33-5-35-00-26-19
Fax: +33-5-61-19-30-00
E-mail: yuval.harness@inria.fr

inverse problems, such as tomography where the visual representation of some hidden object is constructed by partial, and possibly noisy, measurements [25].

The common practice for quantifying uncertainty in computational models, is employ to the parametric method. The theoretical basis for the method was laid down by Wiener [32]. The method itself was initially developed by Ghanem and Spanos [9], and later generalized by Xiu and Karniadakis [28,35,36]. In this approach the uncertain parameters are replaced by random quantities, and the problem is recast as a system with random input. The solution is estimated via global expansion of the random variables into a basis of uncorrelated functions. Thus, the stochastic problem is transformed into a deterministic system in higher dimension. The most popular expansions employed are the *Karhunen-Loève expansion*, and the *generalized Polynomial Chaos* (gPC) expansion.

The parametric approach, often, demonstrates superior performance in terms of computational effort over other traditional methods, see [34] for a detailed review. However, when the physical domain of the problem is uncertain the quantification by the parametric approach becomes much more challenging. The main difficulty stems from the need to employ an accurate discretization which captures desired features of the solution for any realization of the random shape. Producing a family of physical discretization schemes even for a selected finite set of random realizations, generally, requires a considerable effort. The latter is especially true when the geometry undergoes complicated changes as a function of the random parameters. Note, that a single deterministic computation for a specific realization, typically, requires a large computational effort as well.

To overcome the difficulties associated with the quantification of random shape or domain, various techniques have been proposed. Typically, these are classified as one of the following: perturbation, fictitious domain, level-set or random domain mapping. Perturbation techniques [29] are straightforward and simple to apply, however, their applicability is limited to small shape deformations. The fictitious domain [3] and level-set methods [22,23] are based on embedding the random domain in a larger, deterministic domain containing all possible realizations. These methods are capable of handling very irregular non-smooth geometries. However, the embedding introduces non-smoothness in the spatial region, that intersects with the random boundary. Thus, high-order convergence is only partially ensured in the entire computational domain.

The random domain mapping method [26,27] is the most common tool used for solving PDEs on uncertain domains. The method is based on a realization-dependent coordinate transformation uniformly mapping all the realizations of the domain to a fixed, reference configuration. The variational formulation of the PDE on the random domain can then be posed on the reference domain, reducing the problem to a PDE on a fixed domain with stochastic coefficients. The transformed PDE whose domain is fixed is solved using standard techniques. However, the method is highly sensitive to the non-linear dependence of the problem on the random boundary. In case of complex evolution of the shape, the random coefficients can exhibit highly varying behavior. Even worse, non-smoothness of the boundaries can produce singularities which require non-trivial treatment. To overcome these difficulties a very accurate discretization grid is typically imposed, often combined with dimensionality reduction techniques, e.g., sparse grids, to ensure reasonable computational effort. See [4,11,14] for further details.

In this work an alternative method that attempts to mitigate the difficulties associated with the more standard techniques for PDEs on uncertain domains is proposed. The method is of boundary integral type [5] and, thus, can handle large shape deformations with great ease. Our analysis is based on the observation that as a function of the random interface the solution is piece-wise smooth in the spatial domain, i.e., $\mathbb{R}^2$ or $\mathbb{R}^3$. The proposed method constructs a discretization grid of the random surface for all possible realizations in two stages. In the first stage a spatial low-dimensional embedding of the family of random surfaces is constructed via the *Coarea formula* [8]. The embedding, essentially, captures any irregular behavior of the random surface and a discretization is applied only on a compact region in $\mathbb{R}^2$ or $\mathbb{R}^3$. In the second stage a parametric grid corresponding to the low-dimensional spatial grid is imposed. A sparse or hierarchical parametric grid can be applied for dealing with high dimensionality, while the spatial grid effectively ensures that the bulk variation of output functionals defined on the boundary is captured. In general, the method allows the handling of non-trivial geometries without the loss of accuracy in the region intersecting with the random interface.

Since this is a first case study and for the ease of presentation, the discussion has been limited to time-harmonic wave scattering by star-shaped obstacles. In the analysis and numerical study a $2D$ scattering object and low-dimensional parametric space are assumed. More complicated examples in higher spatial and parametric dimensions are discussed. However, in-depth study of this topic is deferred to future work. For its simplicity, acoustic fluid-structure interaction has been chosen as the physical application. In that case, the solution represents small oscillations of pressure in a compressible ideal fluid. The method and ideas presented in this work can also be applied to electrodynamics and elastodynamics.

This work employs the null-field approach [20,30,31,33], which in contrary to the better known *boundary element method* (BEM) [24] and the Nyström method [16], does not involve singular integrals. Null-field methods are fast and much easier to implement compared to BEM and the Nyström method. Their applicability range, however, is typically limited to relatively low wavenumbers. The null-field reconstruction technique [1,13] is inherently stable, admits a-priori error evaluation, and facilitates the extraction of features of interest without prior estimation of the entire solution. The method enables us to perform analysis from a purely geometric point of view, which avoids the additional complications associated with integration of weakly singular kernels. Combining low-dimensional surface embedding with BEM and Nyström method can be foreseen in a future study.

The paper is organized as follows. The fundamentals of the null-field reconstruction method for the time-harmonic wave scattering problem is presented in Section 2. Section 3 reviews the procedure of optimal reconstruction from a numerical linear algebra point of view. Section 4 consists of the main theoretical results of this work and includes the formulation of the problem. In Section 5 the proposed method is applied to the general class of randomly shaped polygonal cylinders, as a proof of concept that the suggested method can, indeed, handle complex non-smooth shapes. Summary of the results as well as suggestions for applying the method in more complicated scenarios are given in Section 6.

2 Null-Field Reconstruction for Time Harmonic Wave Scattering

In this section a brief review on the null-field reconstruction method for the time-harmonic wave scattering problem is given. First the time-harmonic acoustic scattering problem is presented, after which follows a review of the fundamental theory of null-field methods. In the final part the main idea of the null-field reconstruction technique for time-harmonic wave scattering is presented.

2.1 Acoustic Scattering by Impenetrable Obstacles

Let $\mathcal{B}$ denote a bounded domain in $\mathbb{R}^d$ representing an impenetrable obstacle with boundary $\mathcal{S}$, where $d = 2$ or 3. We denote by $\overline{\mathcal{B}} = \mathcal{B} \cup \mathcal{S}$ the closure of $\mathcal{B}$. Let $\mathbb{R}^d \setminus \overline{\mathcal{B}}$ be the unbounded exterior region occupied by a uniform medium. Let $\mathbf{r} \in \mathbb{R}^d$ denote a general spatial point,

$$\mathbf{r} = \begin{cases} (r\cos\theta, r\sin\theta)\,, & \text{if } d = 2\,, \\ (r\sin\varphi\cos\theta, r\sin\varphi\sin\theta, r\cos\varphi)\,, & \text{if } d = 3\,. \end{cases}$$

For an incident time-harmonic field $u^{\mathrm{inc}}(\mathbf{r})$ 'illuminating' the obstacle, the scattered field $u^{\mathrm{sca}}(\mathbf{r})$ satisfies the following exterior boundary value problem:

$$\Delta u^{\mathrm{sca}} + \kappa^2 u^{\mathrm{sca}} = 0 \quad \forall\, \mathbf{r} \in \mathbb{R}^d \setminus \overline{\mathcal{B}}\,, \tag{1}$$

$$u^{\mathrm{sca}} = -u^{\mathrm{inc}} \text{ or } \partial_\nu u^{\mathrm{sca}} = -\partial_\nu u^{\mathrm{inc}} \quad \text{on} \quad \mathcal{S}\,, \tag{2}$$

$$r^{\frac{d-1}{2}} \left(\partial_r u^{\mathrm{sca}} - \mathtt{i}\kappa u^{\mathrm{sca}}\right) \to 0 \quad \text{as} \quad r \to \infty\,, \tag{3}$$

where $\mathtt{i} = \sqrt{-1}$. Equation (1) is known as the *Helmholtz* equation, where Δ is the Laplacian and κ is the *wavenumber*. Equation (2) specifies the boundary condition, depending on the physical problem: adopting the acoustic terminology, it is *sound-soft* for Dirichlet problems and *sound-hard* for Neumann problems. Here ν is the unit outward normal to $\mathcal{S}$ and $\partial_\nu u$ is the normal derivative of u. The last condition (3), known as the *Sommerfeld radiation condition*, ensures that the scattered field propagates from the obstacle to infinity. The solution of the exterior scattering problem is unique. A solution to Helmholtz equation is called a *wavefunction*. A wavefunction satisfying the Sommerfeld condition (3) is called an *outgoing* wavefunction.

2.2 Null-Field Theory Fundamentals

Null-field methods for the acoustic scattering problem (1) are based on Green's second theorem

$$\iint_{\mathcal{R}} (w\Delta v - v\Delta w)\, \mathrm{d}V = \int_{\mathcal{S}} \left(w\frac{\partial v}{\partial \nu} - v\frac{\partial w}{\partial \nu} \right) \mathrm{d}\mathcal{S}\,, \tag{4}$$

which holds for any bounded domain $\mathcal{R}$ with a Lipschitz piecewise smooth boundary $\mathcal{S}$, where v and w are scalar fields, and $\partial v/\partial\nu$ and $\partial w/\partial\nu$ denote corresponding normal derivatives.

Let ψ be an outgoing wavefunction and let u denote the total field, $u^{\mathrm{inc}}+u^{\mathrm{sca}}$. Assuming ψ is analytic in $\mathbb{R}^d \setminus \overline{\mathcal{B}}$, it can be shown by (4) that

$$\int_{\mathcal{S}} \left(u\frac{\partial \psi}{\partial \nu} - \psi \frac{\partial u}{\partial \nu} \right) \mathrm{d}\mathcal{S} = \int_{\mathcal{S}} \left(u^{\mathrm{inc}}\frac{\partial \psi}{\partial \nu} - \psi \frac{\partial u^{\mathrm{inc}}}{\partial \nu} \right) \mathrm{d}\mathcal{S}\,.$$

Thus, for a sound-soft obstacle ($u=0$ on S)

$$\int_{\mathcal{S}} \psi\frac{\partial u}{\partial \nu} \,\mathrm{d}\mathcal{S} = -\int_{\mathcal{S}} \left(u^{\mathrm{inc}}\frac{\partial \psi}{\partial \nu} - \psi \frac{\partial u^{\mathrm{inc}}}{\partial \nu} \right) \mathrm{d}\mathcal{S}\,, \tag{5}$$

while for a sound-hard obstacle ($\partial_\nu u=0$ on S)

$$\int_{\mathcal{S}} u\frac{\partial \psi}{\partial \nu} \,\mathrm{d}\mathcal{S} = \int_{\mathcal{S}} \left(u^{\mathrm{inc}}\frac{\partial \psi}{\partial \nu} - \psi \frac{\partial u^{\mathrm{inc}}}{\partial \nu} \right) \mathrm{d}\mathcal{S}\,. \tag{6}$$

Using (5) or (6) an infinite set of equations can be produced, from which u or $\partial_\nu u$ on $\mathcal{S}$ are approximated. In practice, one chooses a finite subset of equations of the form of (5) and (6) which are employed to optimally reconstruct the scattered field without an explicit estimation of u or $\partial_\nu u$ on $\mathcal{S}$. The core idea of reconstruction by functionals is presented in the next subsection, while the numerical procedure for its practical implementation is covered in Section (3).

2.3 Reconstruction of Surface Functionals

Typically we are interested in estimating features of interest which are expressed by the unknown surface density, u or $\partial_\nu u$ on $\mathcal{S}$. Often such features are the outcomes of functionals in an appropriate *Hilbert space*. Indeed, let h denote the complex conjugate of u or $\partial_\nu u$ on $\mathcal{S}$. Then for a general non-smooth surface $\mathcal{S}$, the surface density h belongs to the complex Hilbert space $\mathcal{L}^2_{\mathrm{d}\mathcal{S}}(\mathcal{S})$ whose inner-product and norm are defined by

$$\langle g\,,h\rangle_{\mathcal{L}^2_{\mathrm{d}\mathcal{S}}} = \int_{\mathcal{S}} h^*(\mathbf{r})g(\mathbf{r})\,\mathrm{d}\mathcal{S}\,, \quad \|h\|_{\mathcal{L}^2_{\mathrm{d}\mathcal{S}}} = \sqrt{\langle h\,,h\rangle_{\mathcal{L}^2_{\mathrm{d}\mathcal{S}}}}\,,$$

where h^* denotes the complex conjugate of h and $\mathrm{d}\mathcal{S}$ is the induced volume form on the surface. Recall that by *Riesz representation theorem* any bounded linear functional $\mathcal{L}^2_{\mathrm{d}\mathcal{S}} \to \mathbb{C}$ operating on surface densities, is of the form $\langle f\,,h\rangle_{\mathcal{L}^2_{\mathrm{d}\mathcal{S}}}$. We call such functionals *surface functionals*.

In this work we focus on the estimation of the *scattering coefficients* of the expansion of u^{sca} to cylinder or spherical harmonics in the $2D$ or $3D$ cases, respectively. These coefficients, denoted by b_m or b_n^m, satisfy

$$u^{\mathrm{sca}}(\mathbf{r}) = \begin{cases} \sum_{m=-\infty}^{\infty} b_m \mathrm{H}_m(\kappa r)e^{\mathrm{i}m\theta} & \text{if } d=2\,, \\ \sum_{n=0}^{\infty}\sum_{m=-n}^{n} b_n^m \mathrm{h}_n^{(1)}(\kappa r)Y_n^m\left(\hat{\mathbf{r}}\right) & \text{if } d=3\,, \end{cases}$$

where $\mathrm{H}_m(z)$ denotes the mth-order *Hankel function of the first kind*, $\mathrm{h}_n^{(1)}(z)$ is the nth-order *spherical Hankel function of the first kind*, and

$$Y_n^m = P_n^m\left(\cos\varphi\right)e^{\mathrm{i}m\theta}\,,$$

where P_n^m are the *associated Legendre functions*. See [5] for further details. The scattering coefficients are very useful features of the surface density, since they can easily express other important quantities such as the *far-field pattern* and the *radar cross section* [12].

Consider the sound-soft case (5). Using the Hilbert space notation, it follows that the scattering coefficients for the $2D$ and $3D$ cases satisfy

$$\frac{\mathtt{i}}{4}\left\langle \mathrm{J}_m(\kappa r)e^{-\mathtt{i}m\theta}\,,\,\partial_\nu u^*(\mathbf{r})\right\rangle_{\mathcal{L}^2_{\mathrm{d}\mathcal{S}}} = b_m\,,\qquad \forall\, m\in\mathbf{Z}\,, \tag{7}$$

$$-\left\langle \mathrm{j}_n(\kappa r)P_n^{|m|}(\cos\varphi)e^{\mathtt{i}m\theta}\,,\,\partial_\nu u^*(\mathbf{r})\right\rangle_{\mathcal{L}^2_{\mathrm{d}\mathcal{S}}} = b_n^m\,,\quad \forall\, 0\le|m|\le n\in\mathbf{Z}^+\,, \tag{8}$$

respectively, where $\mathrm{J}_m(z)$ denotes the mth-order *Bessel function of the first kind*, $\mathrm{j}_n(z)$ is the nth-order *spherical Bessel function of the first kind*, and $\partial_\nu u^*(\mathbf{r})$ denotes the complex conjugate of the surface density $\partial_\nu u(\mathbf{r})$. In practice only $\{b_m\}_{|m|\le\mu}$ satisfying

$$\mu=\lceil 3\kappa r_{\max}\rceil\,,\quad \rho^{\max}=\inf\left\{|\mathbf{r}|\;\middle|\;\mathbf{r}\in\mathbb{R}^d\setminus\overline{\mathcal{B}}\right\}\,, \tag{9}$$

are required for an accurate description of u^{sca}, see [13] for more details. Similar expressions can be derived for the sound-hard case.

The core idea of the reconstruction procedure is to approximate the outcome of target functionals (7) and (8) without producing an explicit approximation of the surface density $\partial_\nu u$ on $\mathcal{S}$. This, generally, allows us to handle much more accurately complex geometries as well as irregular or singular surface densities. Explicitly, we approximate the outcomes (7) and (8) by linear combinations of the following form

$$\frac{\mathtt{i}}{4}\left\langle \mathrm{J}_m(\kappa r)e^{-\mathtt{i}m\theta}\,,\,\overline{\partial_\nu u}\right\rangle_{\mathcal{L}^2_{\mathrm{d}\mathcal{S}}} \approx \left\langle \sum c_{m,l}\psi_\ell^{2\mathrm{D}}\,,\,\overline{\partial_\nu u}\right\rangle_{\mathcal{L}^2_{\mathrm{d}\mathcal{S}}}\,,$$

$$-\left\langle \mathrm{j}_n(\kappa r)P_n^{|m|}(\cos\varphi)e^{\mathtt{i}m\theta}\,,\,\overline{\partial_\nu u}\right\rangle_{\mathcal{L}^2_{\mathrm{d}\mathcal{S}}} \approx \left\langle \sum c_{m,l}\psi_\ell^{3\mathrm{D}}\,,\,\overline{\partial_\nu u}\right\rangle_{\mathcal{L}^2_{\mathrm{d}\mathcal{S}}}\,,$$

where $\{\psi_\ell^{2\mathrm{D}}\}$ and $\{\psi_\ell^{3\mathrm{D}}\}$ are predetermined sets of functionals, in $2D$ and $3D$ respectively, whose outputs are either known or can be calculated directly. We call such functionals the *information functionals*.

As shown in (5) the outcome of the information functionals are readily available if $\psi_\ell^{2\mathrm{D}}$ and $\psi_\ell^{3\mathrm{D}}$ are outgoing wavefunctions whose singularities are located in $\overline{\mathcal{B}}$. Hence, given the information

$$\left\langle \psi_\ell^{2\mathrm{D}}\,,\,\overline{\partial_\nu u}\right\rangle_{\mathcal{L}^2_{\mathrm{d}\mathcal{S}}} = a_\ell^{2\mathrm{D}}\,,\quad \left\langle \psi_\ell^{3\mathrm{D}}\,,\,\overline{\partial_\nu u}\right\rangle_{\mathcal{L}^2_{\mathrm{d}\mathcal{S}}} = a_\ell^{3\mathrm{D}}\,,$$

the outcome of the target functional can be approximate by

$$\frac{\mathtt{i}}{4}\left\langle \mathrm{J}_m(\kappa r)e^{-\mathtt{i}m\theta}\,,\,\overline{\partial_\nu u}\right\rangle_{\mathcal{L}^2_{\mathrm{d}\mathcal{S}}} \approx \sum c_{m,l}a_\ell^{2\mathrm{D}}\,,\quad \forall\, m\in\mathbf{Z}\,,$$

and

$$-\left\langle \mathrm{j}_n(\kappa r)P_n^{|m|}(\cos\varphi)e^{\mathtt{i}m\theta}\,,\,\overline{\partial_\nu u}\right\rangle_{\mathcal{L}^2_{\mathrm{d}\mathcal{S}}} \approx \sum c_{m,l}a_\ell^{3\mathrm{D}}\,,\quad \forall\, 0\le|m|\le n\in\mathbf{Z}^+\,.$$

Obtaining the coefficients $\{c_{m,\ell}\}$ while ensuring measurable error bounds of the estimations of the scattering coefficients can be achieved by *reconstruction kernel* approximation which is the main topic of Section (3).

3 Optimal Reconstruction with A-priori Error Estimate

In this section the procedure of recovery of target functionals by information functionals in general Hilbert space setting is reviewed. Reconstruction problems often involve regularization parameters which govern the stability and accuracy of the procedure. The result of the optimization of the reconstruction with respect to the regularization parameters is referred to as optimal reconstruction. Optimal reconstruction can be traced back to the notion of optimal recovery [10,21]. A more modern analysis from an inverse problem point of view can be found in [17,18,19].

We begin with the definition of the reconstruction problem and the notion of reconstruction kernel. This is followed by a brief description of the numerical procedure including error analysis. The final part elaborates on proper numerical integration rules, that are needed for the error estimates. The method and error analysis presented here, as well as further technical details have been initially introduced in [13].

3.1 The Reconstruction Problem and Reconstruction Kernels

Let $\mathcal{H}$ be a complex Hilbert space, whose inner-product is denoted by $\langle\,,\,\rangle_{\mathcal{H}}$. The reconstruction problem is to approximate a finite set of target functionals

$$\langle g_m\,, h\rangle_{\mathcal{H}} = b_m\,, \quad g_m \in \mathcal{H}\,, \quad m = 1, 2, \ldots, M\,, \tag{10}$$

by a given finite set of information functionals,

$$\langle f_\ell\,, h\rangle_{\mathcal{H}} = a_\ell\,, \quad f_\ell \in \mathcal{H}\,, \quad l = 1, 2, \ldots, L\,, \tag{11}$$

where the element $h \in \mathcal{H}$ is unknown.

Definition 1 Let $\|\ \|_{\mathcal{H}}$ denote the norm induced by $\langle\,,\,\rangle_{\mathcal{H}}$ in $\mathcal{H}$, and let $\mathcal{C}_m^L$ denote a closed convex subset of $\mathbb{C}^L$. A linear combination $\sum_{\ell=1}^L \widehat{c}_{m,\ell} f_\ell$ whose coefficients $(\widehat{c}_{m,1}, \ldots, \widehat{c}_{m,L}) \subset \mathcal{C}_m^L$ satisfy the minimality condition

$$\left\| g_m - \sum_{\ell=1}^L \widehat{c}_{m,\ell} f_\ell \right\|_{\mathcal{H}} \leq \left\| g_m - \sum_{\ell=1}^L c_{m,\ell} f_\ell \right\|_{\mathcal{H}} \quad \forall\, (c_{m,1}, \ldots, c_{m,L}) \in \mathcal{C}_m^L\,, \tag{12}$$

is called an *optimal reconstruction kernel* of the target functional g_m by the information functionals $\{f_\ell\}$ over $\mathcal{C}_m^L$.

Remark 1 Clearly, (12) is a projection on a convex set. The key point which is addressed later, is how to determine the convex set $\mathcal{C}_m^L$. Note that almost no prior knowledge on the element h is assumed.

We will show in the next subsection, that obtaining (12) vastly exceeds our needs. In practice, it is sufficient to obtain an approximation satisfying

$$\left\| g_m - \sum_{\ell=1}^L \widehat{c}_{m,\ell} f_\ell \right\|_{\mathcal{H}} \leq \epsilon\, \|g_m\|_{\mathcal{H}} \quad (\widehat{c}_{m,1}, \ldots, \widehat{c}_{m,L}) \in \mathcal{C}_m^L\,, \tag{13}$$

with respect to some predetermined threshold, $\epsilon > 0$. In that case the linear combination $\sum_{\ell=1}^L \widehat{c}_{m,\ell} f_\ell$ is simply called a *reconstruction kernel* (i.e., not optimal).

3.2 The Discrete Reconstruction Procedure with Error Analysis

For the evaluation of the reconstruction kernel, we assume a finite dimensional discretization satisfying the following definition.

Definition 2 Let $\mathcal{H}_B$ be a bounded subset of a Hilbert space $\mathcal{H}$ whose inner-product is denoted by $\langle\ ,\ \rangle_{\mathcal{H}}$. A mapping,

$$T_{\mathcal{H}_B} : \mathcal{H}_B \to \mathbb{C}^{1\times P}\,, \quad P \in \mathbb{N}\,,$$

is called an inner-product preserving discretization of $\mathcal{H}_B$ of accuracy $\epsilon_{\rm dis} > 0$ if

$$\left|\overrightarrow{f}\,\overrightarrow{g}^{\,*} - \langle f, g\rangle_{\mathcal{H}}\right| < \epsilon_{\rm dis}\,, \quad \forall\, f, g \in \mathcal{H}_B\,, \tag{14}$$

where $\overrightarrow{f} = T_{\mathcal{H}_B}(f)$ and $\overrightarrow{g} = T_{\mathcal{H}_B}(g)$. The vectors $\overrightarrow{f}$ and $\overrightarrow{g}$ are called the corresponding inner-product preserving discretizations of f and g on $\mathcal{H}_B$.

Let $\overrightarrow{f_\ell}, \overrightarrow{g_m} \in \mathbb{C}^{1\times P}$ denote inner-product preserving discretizations of some $f_\ell, g_\ell \in \mathcal{H}_B$, respectively. Let $\eta \in \mathcal{H}$ denote the orthogonal projection of h on the subspace spanned by $\mathcal{H}_B$. By definition (2) we obtain

$$\left|\overrightarrow{f_\ell}\,\overrightarrow{\eta}^{\,*} - \langle f_\ell\,,\, h\rangle_{\mathcal{H}}\right|\,, \left|\overrightarrow{g_m}\,\overrightarrow{\eta}^{\,*} - \langle g_m\,,\, h\rangle_{\mathcal{H}}\right| \le \|\eta\|\epsilon_{\rm dis}\,,$$

for all $\ell \in \{1, 2, \ldots, L\}$ and $m \in \{1, 2, \ldots, M\}$. Hence, given the information (11) and an approximation of $\overrightarrow{g_m}$,

$$\widehat{g}_m = \sum_{\ell=1}^{L} \widehat{c}_{m,\ell}\,\overrightarrow{f_\ell}\,, \tag{15}$$

we can reconstruct the unknown target coefficients (10) via

$$b_m = \langle g_m\,,\, h\rangle_{\mathcal{H}} \approx \widehat{g}_m\,\overrightarrow{\eta}^{\,*} = \sum_{\ell=1}^{L} \widehat{c}_{m,\ell}\,\overrightarrow{f_\ell}\,\overrightarrow{\eta}^{\,*} \approx \sum_{\ell=1}^{L} \widehat{c}_{m,\ell} a_\ell\,. \tag{16}$$

To evaluate the error of the reconstruction (16) we denote for each $\ell = 1, 2, \ldots, L$ and $m = 1, 2, \ldots, M$ the discretization errors

$$\epsilon_\ell = \langle f_\ell\,, h\rangle_{\mathcal{H}} - \overrightarrow{f_\ell}\,\overrightarrow{\eta}^{\,*}\,, \delta_m = \langle g_m\,, h\rangle_{\mathcal{H}} - \overrightarrow{g_m}\,\overrightarrow{\eta}^{\,*}\,,$$

and obtain the following estimate

$$b_m - \sum_{\ell=1}^{L} \widehat{c}_{m,\ell} a_\ell = \delta_m + (\overrightarrow{g_m} - \widehat{g}_m)\,\overrightarrow{\eta}^{\,*} + \sum_{\ell=1}^{L} \widehat{c}_{m,\ell}\epsilon_\ell\,,$$

where our assumption ensure that $|\delta_m|, |\epsilon_\ell| \le \|\eta\|\epsilon_{\rm dis}$. Note that $(\overrightarrow{g_m} - \widehat{g}_m)\,\overrightarrow{\eta}^{\,*}$ is the projection error which can not be reduced if the set of information functionals, $\{f_\ell\}$, is predetermined.

To control the error we impose the following regularization constraint

$$|\widehat{c}_{m,\ell}| \le \epsilon_{\rm evl}/\epsilon_{\rm dis}\,, \quad \epsilon_{\rm evl} \ge \epsilon_{\rm dis}\,, \tag{17}$$

where ϵ_{evl} is a chosen or given evaluation error bound. Thus, we obtain

$$\left| b_m - \sum_{\ell=1}^{L} \widehat{c}_{m,\ell} a_\ell \right| \leq \|\eta\| \cdot \epsilon_{\text{dis}} + \left| (\overrightarrow{g_m} - \widehat{g}_k)\, \overrightarrow{\eta}^* \right| + L \cdot \|\eta\| \cdot \epsilon_{\text{evl}} \,. \tag{18}$$

The regularization constraint (17) explicitly defines the convex set $\mathcal{C}_m^L$ in (12) as

$$\mathcal{C}_m^L = \left\{ (c_1, c_2, \ldots, c_L) \;\middle|\; |c_\ell| \leq \frac{\epsilon_{\text{evl}}}{\epsilon_{\text{dis}}} \right\} .$$

The error estimate (18) implies that it is sufficient to obtain an approximation (15) satisfying $\|(\overrightarrow{g_m} - \widehat{g}_k)\| \leq \epsilon_{\text{evl}}$. Indeed, in that case (18) reduces to

$$\left| b_m - \sum_{\ell=1}^{L} \widehat{c}_{m,\ell} a_\ell \right| \leq \|\eta\| \cdot \epsilon_{\text{dis}} + (L+1) \cdot \|\eta\| \cdot \epsilon_{\text{evl}} \,.$$

Often, the summation of evaluation errors $\sum_{\ell=1}^{L} \widehat{c}_{m,\ell} \epsilon_\ell$ is not cumulative. Thus, the overall error is typically $\mathcal{O}(\epsilon_{\text{evl}})$ assuming $\|\eta\| = \mathcal{O}(1)$. This facilitates an efficient approximation technique which is based performing successive *singular value decompositions* on subsets of information functionals. The technique was presented in [13] and demonstrated high stability and good convergence properties. Further details including different variants of the technique can be found in [12].

3.3 Inner-Product Preserving Discretization and Numerical Integration

Obtaining inner-product preserving discretizations of surface functionals is a fundamental issue. Let us focus on the case, as in this work, where $\{f_\ell\}$ and $\{g_m\}$ are smooth functions in some $\mathcal{H} = \mathcal{L}^2$ space with an inner-product,

$$\langle f \,,\, g \rangle_{\mathcal{H}} = \int_{\mathcal{D}} f g^* \, \omega \, \mathrm{d}s \,,$$

where $\mathcal{D} \subset \mathbb{R}^d$ is compact and Jordan measurable, g^* is the complex conjugate of g and ω is a proper *weight function*.

We compute the integrals by a numerical integration, typically by some standard rule of the form

$$\langle f, g \rangle_{\mathcal{H}} \approx \sum_{i=1}^{N} f(\sigma^{(i)}) g^*(\sigma^{(i)}) \omega^{(i)} \,,$$

with *integration nodes* $\sigma^{(1)}, \ldots, \sigma^{(N)}$ contained in $\mathcal{D}$ and real positive weights $\omega^{(1)}, \ldots, \omega^{(N)}$. Discretizing an element $f \in \mathcal{H}$ as a weighted *gridfunction*

$$\overrightarrow{f} = \left(f(\sigma^{(1)}) \sqrt{\omega^{(1)}}, \ldots, f(\sigma^{(M)}) \sqrt{\omega^{(N)}} \right) ,$$

essentially, satisfies the inner-product preserving assumption (14) if $N \in \mathbb{N}$ is sufficiently large. The number of elements N required for an effective inner-product preserving discretization depends on the convergence rate of the numerical integration formula and, typically, under some smoothness assumption of the integrands. Indeed, if the weight function ω encompasses all the singularities while $f(s)$ and $g(s)$ are analytic, a *Gaussian* numerical integration rule with respect ω, essentially, ensures exponential convergence. Note that the weights of Gaussian rules are always positive and uniformly bounded. See [6] for more details.

4 Surface Embedding of 2D Random Star-Shaped Obstacles

In this section the main theoretical contribution of this paper is presented. The first two subsections cover the setting of the problem, where Subsection (4.1) defines the random shape properties, and Subsection (4.2) covers the relevant components *generalized Polynomial Chaos* (gPC) expansion theory. The chosen framework leads to a reconstruction problem in a Hilbert space. A concise discussion on the disadvantages of naive discretization of the reconstruction problem concludes Subsection (4.2).

In Subsection (4.3) we present an analytic approach for overcoming the difficulties associated with the naive discretization approach. Using the Coarea formula we construct a low-dimensional spatial embedding within the family of random surfaces, which facilitates a natural choice for setting a cubature rule in a compact region of $\mathbb{R}^2$. The chosen integration weight function is a strictly positive minimal variance quantity encompassing the irregularities of the family of random surfaces.

In Subsection (4.4) we focus on the case of a single random variable describing the randomness of the object. Using the *implicit function theorem* we obtain explicit formulas including full characterization of the singular behavior of the integration weight function. The usage of the single random variable formulation as a building block for the more general case of multiple random variables is considered and discussed in Section (6).

Subsections (4.5) and (4.6) are devoted to the demonstration of the preceding theoretical parts on a model problem of a randomly oriented elliptic cylinder. The random orientation problem is a very simple 'toy' problem. However, it allows us us to demonstrate in a lucid and affable fashion the theoretical ingredients.

4.1 The 2D Random Shape Setting

For brevity, we focus on the sound-soft case and assume that $\mathcal{B}$ represents a star-shaped obstacle in $\mathbb{R}^2$ whose boundary, $\mathcal{S}$, depends smoothly on a real valued vector of mutually independent and continuous random variables

$$\mathbf{Z} = (Z_1, \ldots, Z_P)\,, \quad P \in \mathbb{N}\,.$$

The boundary $\mathcal{S}$ is, however, not assumed to be uniformly smooth in the spatial domain. We assume that each random variable Z_p has finite even moments

$$\mathbb{E}\left[{Z_p}^{2n}\right] = \int_{\mathcal{I}_{Z_p}} z_p^{2n} \frac{dF_{Z_p}}{dz_p}\,\mathrm{d}z_p < \infty\,, \quad n \in \{0, 1, \ldots, N\}\,, \tag{19}$$

where $\mathcal{I}_{Z_p}$ is the support of Z_p and $\frac{dF_{Z_p}(z_p)}{dz_p}$ is the *probability density function* of Z_p. The property (19) effectively ensures the existence of surface functionals suitable for the reconstruction of the scattering coefficients.

Our assumption that the obstacle is star-shaped for any realization of the random vector $\mathbf{Z}$, ensures that its boundary possesses a polar representation,

$$\mathcal{S}(\mathbf{Z}) = \{\, (\rho(\theta;\mathbf{Z})\cdot\cos\theta, \rho(\theta;\mathbf{Z})\cdot\sin\theta) |\ \theta \in [0, 2\pi]\}\,, \tag{20}$$

and the existence of two positive radial bounds, $\rho^{\max}$ and $\rho^{\min}$, satisfying

$$0 < \rho^{\min} = \inf_{\theta,\mathbf{z}} \rho(\theta;\mathbf{z}) < \sup_{\theta,\mathbf{z}} \rho(\theta;\mathbf{z}) = \rho^{\max} < \infty\,. \tag{21}$$

Thus, as illustrated in Figure (1), $\mathcal{S}(\mathbf{Z})$ is confined to the transition region,

$$\mathcal{R}^{\mathrm{tra}} = \left\{ \mathbf{r} \in \mathbb{R}^2 \;\middle|\; \rho^{\min} < |\mathbf{r}| < \rho^{\max} \right\} \subset \mathbb{R}^2\,. \tag{22}$$

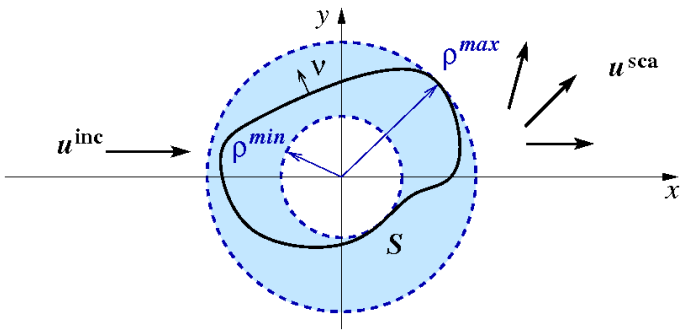

Fig. 1: **The Transition Region $\mathcal{R}^{\mathrm{tra}}$.**

4.2 Random Shape and Generalized Polynomial Chaos Expansion

Given our assumptions we observe that the scattering coefficients (7) are finite dimensional *random fields*,

$$b_m = b_m(\mathbf{Z})\,.$$

A common method to approximate these fields is to obtain their generalized Polynomial Chaos (gPC) expansions,

$$b_m(\mathbf{Z}) \approx b_m^N(\mathbf{Z}) = \sum_{|\mathbf{n}|\le N} b_{m,\mathbf{n}} P_{\mathbf{n}}(\mathbf{Z})\,, \tag{23}$$

where $\mathbf{n} = (n_1,\ldots,n_P)$ is a multi-index and $\{P_{\mathbf{n}}\}$ is an orthogonal basis of the inner-product space induced by the probability density function of $\mathbf{Z}$,

$$\langle \phi(\mathbf{Z})\,,\, \psi(\mathbf{Z})\rangle_{\mathcal{L}^2_{\mathrm{dF}_\mathbf{Z}}} = \int_{\mathcal{I}_\mathbf{Z}} \phi(\mathbf{z})\psi(\mathbf{z})\mathrm{dF}_\mathbf{Z}(\mathbf{z})\,, \quad \mathrm{dF}_\mathbf{Z}(\mathbf{z}) = \prod_{\mathrm{k}=1}^{\mathrm{P}} \mathrm{dF}_{\mathrm{Z_p}}(\mathrm{z_p})\,,$$

whose support is $\mathcal{I}_\mathbf{Z} = \mathcal{I}_{Z_1}\times\cdots\times\mathcal{I}_{Z_P}$. Hence, the expansion coefficients are readily available by the orthogonality via

$$b_{m,\mathbf{n}} = \frac{1}{\gamma_\mathbf{n}} \langle b_m\,,\, P_\mathbf{n}\rangle_{\mathcal{L}^2_{\mathrm{dF}_\mathbf{Z}}}\,, \quad \gamma_\mathbf{n} = \langle P_\mathbf{n}\,,\, P_\mathbf{n}\rangle_{\mathcal{L}^2_{\mathrm{dF}_\mathbf{Z}}}\,.$$

For a randomly shaped obstacle each coefficient in the gPC expansion (23) is a target functional of the following form

$$b_{m,\mathbf{n}} = \int_{\mathcal{I}_{\mathbf{Z}}} \int_{\mathcal{S}(\mathbf{z})} g_m(\mathbf{r}) h(\mathbf{z}, \boldsymbol{\rho}) \, \mathrm{d}\mathcal{S}(\mathbf{z}) P_{\mathbf{n}}(\mathbf{z}) \, \mathrm{d}F_{\mathbf{Z}}(\mathbf{z}) \,. \tag{24}$$

Using the polar form representation (20) whose associated induced volume form on the surface is $\mathrm{d}\mathcal{S}(\theta; \mathbf{z}) = \sqrt{\rho^2 + \rho_\theta^2} \, \mathrm{d}\theta$, the general representation (24) can be explicitly written as

$$b_{m,\mathbf{n}} = \int_{\mathcal{I}_{\mathbf{Z}}} \int_{[0,2\pi]} g_m(\boldsymbol{\rho}) h(\mathbf{z}, \theta) s(\theta; \mathbf{z}) \rho \, \mathrm{d}\theta P_{\mathbf{n}}(\mathbf{z}) \, \mathrm{d}F_{\mathbf{Z}}(\mathbf{z}) \,, \tag{25}$$

where the normalized polar metric tensor is given by

$$s(\theta; \mathbf{z}) = \frac{1}{\rho(\theta; \mathbf{z})} \cdot \frac{\partial S(\theta; \mathbf{z})}{\partial \theta} = \sqrt{1 + \left(\frac{1}{\rho} \cdot \frac{\partial \rho}{\partial \theta} \right)^2} \,.$$

In principle, we need to devise a discretization scheme for (25) and apply the optimal reconstruction procedure of Section (3). However, $\boldsymbol{\rho} \in \mathcal{S}(\mathbf{Z})$ inherits any irregularity of family of surfaces; e.g., lack of smoothness and oscillatory behaviour, which often necessitates specialized high-order discretization of the surface $\mathcal{S}(\mathbf{Z})$. Additionally, discretizing the random surface integral with a grid of numerical integration nodes has to be realized for every grid point in the parameters domain, $\mathcal{I}_{\mathbf{Z}}$. Hence, in general, the practical implementation of an inner-product preserving discretization satisfying (14) is a difficult task. An analytic approach for overcoming this fundamental difficulty is presented in the next subsection.

4.3 Random Surface Embedding and the Coarea Formula

In this subsection we present an analytic approach for producing inner-product preserving discretizations of functionals of the form of (25). The key idea is to apply a change of variables transforming (25) to the following equivalent representation

$$b_{m,\mathbf{n}} = \iint_{\mathcal{R}^{\mathrm{tra}}} g_m(\mathbf{r}) \phi_{\mathbf{n}}(h) \omega(\mathbf{r}) r \, \mathrm{d}\theta \, \mathrm{d}r \,, \tag{26}$$

where the weight function $\omega(\mathbf{r}) > 0$, is proportional to the conditional expectation of $s(\theta; z)$ given the information $\boldsymbol{\rho}(\theta; z) = \mathbf{r} \in \mathcal{R}^{\mathrm{tra}}$. Thus, $\omega(\mathbf{r})$ has minimal variance while, essentially, encompassing the irregularities of the family of random surfaces, $\mathcal{S}(\mathbf{Z})$. The term $\phi_{\mathbf{n}}(h)$ is a linear functional uniformly bounded in $\mathcal{R}^{\mathrm{tra}}$ operating on h. A high-order numerical integration rule with respect to $\omega(\mathbf{r})$ would serve as a discretization satisfying (14). The transformed representation (26) is obtained by the so-called *Coarea Formulae* [8] which allows us to express the surface integral in terms of the integral of the level sets of another function.

Theorem 1 *(**The Coarea Formula**)*
Let $\boldsymbol{\Phi} : \mathbb{R}^{d+\delta d} \to \mathbb{R}^d$ *be a piecewise smooth* Lipschitz *function, where* $d \geq 0$. *Let* $\mathcal{D}$ *be an open* Jordan measurable *subset of* $\mathbb{R}^{d+\delta d}$, *then for any integrable function* $g : \mathcal{D} \to \mathbb{R}$,

$$\int_{\mathcal{D}} g(x) = \int_{\mathbb{R}^d} \left(\int_{\boldsymbol{\Phi}^{-1}(y)} \frac{g(x)}{J_{\boldsymbol{\Phi}}(x)} \, d\mathcal{S}_{\boldsymbol{\Phi}^{-1}(y)}(x) \right) dy \,, \tag{27}$$

where $J_{\boldsymbol{\Phi}}(x) = \sqrt{\det\left([D_{\boldsymbol{\Phi}}(x)] \cdot [D_{\boldsymbol{\Phi}}(x)]^T \right)}$ *is the Jacobian of* $\boldsymbol{\Phi}$, *and* $d\mathcal{S}_{\boldsymbol{\Phi}^{-1}(y)}$ *denotes volume density of* $\boldsymbol{\Phi}^{-1}(y)$.

Remark 2 The coarea formula expresses the integral in terms of the integral of the level sets of the function $\boldsymbol{\Phi}$. The level sets, $\boldsymbol{\Phi}^{-1}(y)$, are called fibers of the domain $\mathcal{D}$. The formula is, in fact, a generalization of *Fubini's theorem.*

Let us consider the function

$$\boldsymbol{\Phi}(\mathbf{z}, \theta) = \boldsymbol{\rho}(\theta; \mathbf{z}) = (\rho(\theta; \mathbf{z}) \cdot \cos\theta, \rho(\theta; \mathbf{z}) \cdot \sin\theta) \,, \quad \boldsymbol{\Phi} : \mathcal{I}_{\mathbf{Z}} \times [0, 2\pi] \to \mathcal{R}^{\text{tra}} \,.$$

By direct calculations we obtain

$$D_{\boldsymbol{\Phi}} = \begin{pmatrix} \nabla_{\mathbf{z}}\rho\cos\theta & \nabla_{\mathbf{z}}\rho\sin\theta \\ \partial_\theta(\rho\cos\theta) & \partial_\theta(\rho\sin\theta) \end{pmatrix}^T \in \mathbb{R}^{2\times(P+1)} \,, \quad J_{\boldsymbol{\Phi}} = \rho \cdot |\nabla_{\mathbf{z}}\rho| \,,$$

where

$$\nabla_{\mathbf{z}}\rho = (\partial_{z_1}\rho, \ldots, \partial_{z_P}\rho)^T \,, \quad |\nabla_{\mathbf{z}}\rho|^2 = \sum_{p=1}^{P} \left(\partial_{z_p}\rho\right)^2 \,.$$

Hence, applying (27) on (25) with the chosen implicit function, satisfies

$$b_{m,\mathbf{n}} = \iint_{\mathcal{R}^{\text{tra}}} g_m(\mathbf{r}) \int_{\mathcal{I}_{\mathbf{Z}_\mathbf{r}}} h(\mathbf{z}, \theta) P_{\mathbf{n}}(\mathbf{z}) \frac{s(\theta; \mathbf{z})}{|\nabla_{\mathbf{z}}\rho|} \prod_{p=1}^{P} \frac{\mathrm{d}F_{Z_p}}{\mathrm{d}z_p} \, \mathrm{d}\mathcal{S}_{\mathbf{r}} r \, \mathrm{d}\theta \, \mathrm{d}r \,, \tag{28}$$

where the domain of integration of the inner integral is the fiber set

$$\mathcal{I}_{\mathbf{Z}_\mathbf{r}} = \{ \mathbf{z} \in \mathcal{I}_{\mathbf{Z}} | \, \boldsymbol{\rho}(\theta; \mathbf{z}) = \mathbf{r} \} \subset \mathcal{I}_{\mathbf{Z}} \,. \tag{29}$$

The advantage of the representation (28) is that the wave function, g_m, is no longer composed with the boundary and does not inherit its irregular properties.

The main challenge is to efficiently evaluate the inner integral in (28),

$$\int_{\mathcal{I}_{\mathbf{Z}_\mathbf{r}}} h(\mathbf{z}, \theta) P_{\mathbf{n}}(\mathbf{z}) \frac{s(\theta; \mathbf{z})}{|\nabla_{\mathbf{z}}\rho|} \prod_{k=1}^{K} \frac{dF_{Z_p}}{dz_p} \, \mathrm{d}\mathcal{S}_{\mathbf{r}} \,. \tag{30}$$

This integral can become infinite since $|\nabla_{\mathbf{z}}\rho|^{-1}$ and $\prod_{k=1}^{K} \frac{dF_{Z_p}}{dz_p}$ are, essentially, singular. Accordingly, using the following weight function

$$\omega(\mathbf{r}) = \int_{\mathcal{I}_{\mathbf{Z}_\mathbf{r}}} \frac{s(\theta; \mathbf{z})}{|\nabla_{\mathbf{z}}\rho|} \prod_{k=1}^{K} \frac{dF_{Z_p}}{dz_p} \, \mathrm{d}\mathcal{S}_{\mathbf{r}} \,, \tag{31}$$

we have that

$$b_{m,\mathbf{n}} = \iint_{\mathcal{R}^{\mathrm{tra}}} g_m(\mathbf{r})\phi_{\mathbf{n}}(h)\omega(\mathbf{r})r\,\mathrm{d}\theta\,\mathrm{d}r\,, \tag{32}$$

where

$$\phi_{\mathbf{n}}(h) = \omega^{-1}(\mathbf{r}) \cdot \int_{\mathcal{I}_{\mathbf{Z_r}}} h(\mathbf{z},\theta)P_{\mathbf{n}}(\mathbf{z})\frac{s(\theta;\mathbf{z})}{|\nabla_{\mathbf{z}}\rho|}\prod_{k=1}^{K}\frac{dF_{Z_p}}{dz_p}\,\mathrm{d}\mathcal{S}_{\mathbf{r}}\,, \tag{33}$$

is a linear functional operating on the surface density h. If $\phi_{\mathbf{n}}(h)$ is bounded then the choice (31) ensures that (30) is effectively desingularized.

To show that $\phi_{\mathbf{n}}(h)$ is a bounded linear functional, we observe that (31) is, in fact, proportional to the conditional expectation of $s(\theta;z)$ given $\rho(\theta;\mathbf{z}) = r$,

$$\omega(\mathbf{r}) = \mathbb{E}\left[\,s(\theta;\mathbf{z})|\,\rho(\theta,\mathbf{z}) = r\right] \cdot f_{\rho}(\mathbf{z})\,,$$

where $f_{\rho}(\mathbf{z})$ is the probability density function of $\rho(\theta;\mathbf{Z})$. It is well known that conditional expectation is a minimum variance predictor as a function of the given information. Hence, the choice (31) implies minimization of oscillatory behaviour of $s(\theta;\mathbf{z})$ as a function of $\rho(\theta;\mathbf{z})$. Employing a similar argument we obtain that the linear functional (33) is, in fact,

$$\phi_{\mathbf{n}}(h) = \frac{\mathbb{E}\left[\,h(\mathbf{z},\theta)P_{\mathbf{n}}(\mathbf{z})s(\theta;\mathbf{z})|\,\rho(\theta;\mathbf{z}) = r\right]}{\mathbb{E}\left[\,s(\theta;\mathbf{z})|\,\rho(\theta;\mathbf{z}) = r\right]}\,.$$

Hence, the *Cauchy-Schwarz* inequality implies that

$$|\phi_{\mathbf{n}}(h)| \leq \left(\max_{\mathbf{z}\in\mathcal{I}_{\mathbf{Z_r}}}|P_{\mathbf{n}}(\mathbf{z})|\right) \cdot \mathbb{E}\left[\,|h(\mathbf{z},\theta)|\;|\;\rho(\theta;\mathbf{z}) = r\right]\,,$$

which shows that the linear functional, $\phi_{\mathbf{n}}$, is, indeed, bounded.

Setting the integration grid for (32) can be done in two stages. First we obtain a cubature rule with nodes $\{\mathbf{r}^{(i,j)}\} \subset \mathcal{R}^{\mathrm{tra}}$ and corresponding cubature weights $\{\omega^{(i,j)}\}$ with respect to the weight function $\omega(\mathbf{r})$, regardless of z. In the second stage we identify the integration grid in $\mathcal{I}_{\mathbf{Z_r}}$ which corresponds $\{\mathbf{r}^{(i,j)}\}$ for the evaluation of $\phi_{\mathbf{n}}(h)$.

4.4 Explicit Representation for a Single Random Variable

Let us consider a simplified case of one-dimensional random vector,

$$\mathbf{Z} = Z \in \mathcal{I}_Z \subset \mathbb{R}\,.$$

Then $\mathrm{d}F_{\mathbf{Z}} = \mathrm{d}F_Z$ and the target functional (25) reduces to

$$b_{m,n} = \int_{\mathcal{I}_Z}\int_{[0,2\pi]} g_m(\boldsymbol{\rho})h(z,\theta)s(\theta;z)\rho\,\mathrm{d}\theta P_n(z)\,\mathrm{d}F_Z(z)\,. \tag{34}$$

We will show that in this case the functional $\phi_{\mathbf{n}}(h)$ (33) can be explicitly represented. This approach can serve as a building block for the case of a general random vector, which is discussed in Section (6).

For applying formula (28) we observe that the fiber set $\mathcal{I}_{\mathbf{Z}_\mathbf{r}}$ (29) is, essentially, a finite set of discrete points; i.e., a zero-dimensional sub-surface. Accordingly, we obtain the following explicit representation of (28) for a single random variable,

$$\iint_{\mathcal{R}^{\mathrm{tra}}} g_m(\mathbf{r}) \left[\sum_{z_\mathbf{r} \in \mathcal{I}_{Z_\mathbf{r}}} h(z_\mathbf{r}, \theta) P_n(z_\mathbf{r}) \frac{s(\theta; z_\mathbf{r})}{|\partial_z \rho|_{z=z_\mathbf{r}}} \frac{dF_Z}{dz}(z_\mathbf{r}) \right] r \, \mathrm{d}\theta \, \mathrm{d}r \,, \tag{35}$$

where $\mathcal{I}_{Z_\mathbf{r}}$ is the reduction of $\mathcal{I}_{\mathbf{Z}_\mathbf{r}}$ to a zero dimensional subset of $\mathcal{I}_Z$,

$$\mathcal{I}_{Z_\mathbf{r}}(\mathbf{r}) = \{ z \in \mathcal{I}_Z \mid \rho(\theta; z) = r \} \,. \tag{36}$$

To efficiently evaluate (35), we employ the *implicit function theorem* [7] which ensures the following identities

$$1 = \partial_r \rho(\theta; z_\mathbf{r}) = \left[\partial_z \rho(\theta; z) \right]_{z=z_\mathbf{r}} \partial_r z_\mathbf{r} \,,$$

$$\partial_\theta \rho(\theta; z_\mathbf{r}) = \left[\partial_z \rho(\theta; z) \right]_{z=z_\mathbf{r}} \partial_\theta z_\mathbf{r} + \left[\partial_\theta \rho(\theta; z) \right]_{z=z_\mathbf{r}} \,.$$

Thus,

$$\left[\partial_z \rho(\theta; z) \right]_{z=z_\mathbf{r}} = \frac{1}{\partial_r z_\mathbf{r}} \,, \quad \left[\partial_\theta \rho(\theta; z) \right]_{z=z_\mathbf{r}} = -\frac{\partial_\theta z_\mathbf{r}}{\partial_r z_\mathbf{r}} \,, \tag{37}$$

and (35) can be equivalently represented by

$$\begin{aligned} b_{m,n} &= \iint_{\mathcal{R}^{\mathrm{tra}}} g_m(\mathbf{r}) \left[\sum_{z_\mathbf{r} \in \mathcal{I}_{Z_\mathbf{r}}} h(z_\mathbf{r}, \theta) P_n(z_\mathbf{r}) s(\theta; z_\mathbf{r}) |\partial_r z_\mathbf{r}| \frac{dF_Z}{dz}(z_\mathbf{r}) \right] r \, \mathrm{d}\theta \, \mathrm{d}r \,, \\ &= \iint_{\mathcal{R}^{\mathrm{tra}}} g_m(\mathbf{r}) \left[\sum_{z_\mathbf{r} \in \mathcal{I}_{Z_\mathbf{r}}} h(z_\mathbf{r}, \theta) P_n(z_\mathbf{r}) |\nabla z_\mathbf{r}| \frac{dF_Z}{dz}(z_\mathbf{r}) \right] r \, \mathrm{d}\theta \, \mathrm{d}r \,, \end{aligned} \tag{38}$$

since the gradient of $z_\mathbf{r}$,

$$\nabla z_\mathbf{r} = \hat{x} \partial_x z_\mathbf{r} + \hat{y} \partial_y z_\mathbf{r} = \hat{\mathbf{r}} \partial_r z_\mathbf{r} + \hat{\boldsymbol{\theta}} \frac{1}{r} \partial_\theta z_\mathbf{r} \,,$$

satisfies $|\nabla z_\mathbf{r}| = s(\theta; z_\mathbf{r}) |\partial_r z_\mathbf{r}|$.

By our definitions $s(\theta; z)$ is strictly positive. Hence, the zeros of $\partial_z \rho$ and the singularities of $\frac{dF_Z}{dz}$ define the integration rule in the sense, that we can apply a cubature rule whose weight function captures the singular behaviour of $|\partial_r z_\mathbf{r}| = |\partial_z \rho|^{-1}_{z=z_\mathbf{r}}$ and $\frac{dF_Z}{dz}$. Now, employing (31) yields the following weight function

$$\omega(\mathbf{r}) = \sum_{z_\mathbf{r} \in \mathcal{I}_{Z_\mathbf{r}}} s(\theta; z_\mathbf{r}) |\partial_r z_\mathbf{r}| \frac{dF_Z}{dz}(z_\mathbf{r}) = \sum_{z_\mathbf{r} \in \mathcal{I}_{Z_\mathbf{r}}} |\nabla z_\mathbf{r}| \frac{dF_Z}{dz}(z_\mathbf{r}) \,, \tag{39}$$

which reduces (38) to

$$b_{m,n} = \iint_{\mathcal{R}^{\mathrm{tra}}} g_m(\mathbf{r}) \phi_n(h) \omega(\mathbf{r}) r \, \mathrm{d}\theta \, \mathrm{d}r \,,$$

where the bounded linear functional (33) reduces to

$$\begin{aligned}\phi_n(h) &= \sum_{z_{\mathbf{r}}\in\mathcal{I}_{Z_{\mathbf{r}}}} h(\theta;z_{\mathbf{r}})P_n(z_{\mathbf{r}})\frac{|\nabla z_{\mathbf{r}}|\frac{dF_Z}{dz}(z_{\mathbf{r}})}{\sum_{y_{\mathbf{r}}\in\mathcal{I}_{Z_{\mathbf{r}}}}|\nabla y_{\mathbf{r}}|\frac{dF_Z}{dz}(y_{\mathbf{r}})}\,,\\ &= \sum_{z_{\mathbf{r}}\in\mathcal{I}_{Z_{\mathbf{r}}}} h(\theta;z_{\mathbf{r}})P_n(z_{\mathbf{r}})\left[\sum_{y_{\mathbf{r}}\in\mathcal{I}_{Z_{\mathbf{r}}}\setminus\{z_{\mathbf{r}}\}}|\nabla y_{\mathbf{r}}|\frac{dF_Z}{dz}(y_{\mathbf{r}})\right]^{-1}. \qquad (40)\end{aligned}$$

Once the cubature nodes $\{\mathbf{r}^{(i,j)}\}$ and corresponding weights $\{\omega^{(i,j)}\}$ have been chosen, we must also identify the value of $z_{\mathbf{r}}\in\mathcal{I}_{Z_{\mathbf{r}}}$ at these nodes for the evaluation of $\phi_n(h)$ (40). This, essentially, requires the solution of the following convex minimization problem,

$$\left\{z^{(i,j,k)}\right\} = \underset{|z|\le 1}{\arg\min}\left(\rho(\theta^{(i,j)};z)-r^{(i,j)}\right)^2.$$

Thus, in practice we obtain a cubature grid and corresponding weights

$$\left\{\left(\theta^{(i,j)},z^{(i,j,k)}\right)\right\}\,,\quad \left\{\omega^{(i,j)}\right\}\,,$$

respectively, which apply to the original form (34) in the sense that

$$b_{m,n}\approx\sum_{i,j} g_m(\mathbf{r}^{(i,j)})\phi_n^{(i,j)}r^{(i,j)}\omega^{(i,j)}\,,$$

where $\mathbf{r}^{(i,j)}=\boldsymbol{\rho}(\theta^{(i,j)},z^{(i,j,k)})$ independently of k, and

$$\phi_n^{(i,j)} = \sum_k h(\theta^{(i,j)};z^{(i,j,k)})P_n(z^{(i,j,k)})\left[\sum_{q\neq k}|\nabla z_{\mathbf{r}}|\,\frac{dF_Z}{dz}\right]^{-1}_{z=z^{(i,j,q)}},$$

where $|\nabla z_{\mathbf{r}}|_{z=z^{(i,j,q)}}$ should, generally, be obtained numerically.

4.5 Example: Randomly Oriented Elliptic Cylinder

Let $\mathcal{B}$ be a sound-soft elliptic cylinder with major radius a and minor radius b, i.e., $a>b>0$. The symmetry axis of the cylinder is located at the origin $\mathcal{O}=(0,0)$. The major and minor axes of the elliptic cross-section are assumed to be rotated counter-clockwise by $z\in[0,2\pi]$, see Figure (2). Note, that the radial bounds (21) are $b=\rho^{\min}<\rho^{\max}=a$.

The polar form of the obstacle's boundary over all random orientation states is given by

$$\mathcal{S}(z)=\left\{\,(\rho(\theta-z)\cdot\cos\theta,\rho(\theta-z)\cdot\sin\theta)|\ \theta\in[0,2\pi]\right\}\,,$$

where $\rho(t)\in(b,a)$ satisfies

$$\rho(t)=\frac{ab}{\sqrt{b^2\cos^2 t+a^2\sin^2 t}}\,,\quad \frac{\rho'(t)}{\rho(t)}=\frac{(a^2-b^2)\sin(2t)/2}{b^2\cos^2 t+a^2\sin^2 t}\,.$$

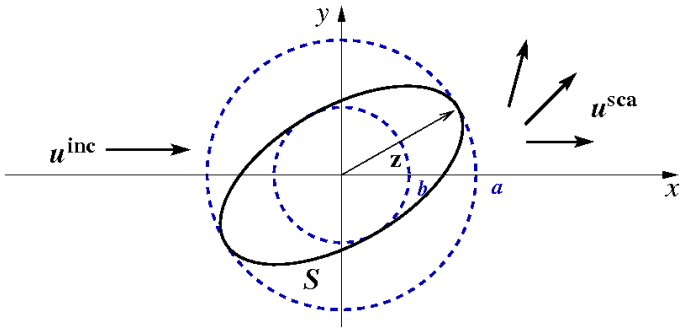

Fig. 2: **Randomly Oriented Elliptic Cylinder.**

Thus, the zeros of $\partial_z \rho(\theta - z)$ are attained at $\theta - z = 0, \pi/2, \pi, 3\pi/2$. Note, that

$$[\rho(\theta - z)]_{\theta - z = 0, \pi} = a\,, \quad [\rho(\theta - z)]_{\theta - z = \pi/2, 3\pi/2} = b\,,$$

which are, indeed, the points of the random surface that do not vary in the radial direction as a function of the parameter z.

The equality $\rho(t) = r$ can be solved analytically which yields

$$\{\rho(t) = r \,|\, r \in (b, a)\} = \{-\zeta\,, \zeta\,, \pi - \zeta\,, -\pi + \zeta\}\,, \tag{41}$$

where

$$\zeta(r) = \arccos\left(\frac{a}{r}\sqrt{\frac{r^2 - b^2}{a^2 - b^2}}\right) \in (0, \pi/2)\,, \quad \forall\, r \in (b, a)\,. \tag{42}$$

Hence, we obtain $\mathcal{I}_{Z_{\mathbf{r}}} = \{z_{\mathbf{r}}^{(1)}, z_{\mathbf{r}}^{(2)}, z_{\mathbf{r}}^{(3)}, z_{\mathbf{r}}^{(4)}\}$ (36) where

$$z_{\mathbf{r}}^{(1)} = \theta - \zeta\,, \quad z_{\mathbf{r}}^{(2)} = \theta + \zeta\,, \quad z_{\mathbf{r}}^{(3)} = \theta - \zeta + \pi\,, \quad z_{\mathbf{r}}^{(4)} = \theta + \zeta - \pi\,,$$

and

$$\frac{\partial z_{\mathbf{r}}^{(k)}}{\partial r} = (-1)^p \frac{d\zeta}{dr} = (-1)^{k+1}\left|\frac{d\zeta}{dr}\right|\,, \quad k = 1, 2, 3, 4\,.$$

Thus, the target functional (38) takes the following form

$$b_{m,n} = \iint_{\mathcal{R}^{\mathrm{tra}}} g_m(\mathbf{r})\left[\sum_{k=1}^{4} h(\theta, z_{\mathbf{r}}^{(k)}) P_n(z_{\mathbf{r}}^{(k)}) \sqrt{1 + \left(\frac{d\zeta}{dr}\right)^2}\, \frac{dF_Z}{dz}(z_{\mathbf{r}}^{(k)})\right] r\, \mathrm{d}\theta\, \mathrm{d}r\,,$$

where

$$\mathcal{R}^{\mathrm{tra}} = \left\{ \mathbf{r} \in \mathbb{R}^2 \;\middle|\; b < |\mathbf{r}| < a \right\}\,.$$

Let us now assume that Z is a uniformly distributed random variable in $[0, 2\pi]$,

$$\mathbb{P}(Z < z_0) = \int_0^{z_0} \frac{\mathrm{dz}}{2\pi} = \frac{z_0}{2\pi}\,.$$

The problem is 2π-periodically smooth in z, hence, it is natural to employ

$$P_0(z) = 1\,, \quad P_n(z) = \begin{cases} \cos(\lfloor n/2 \rfloor \theta) \text{ if } n = 2\lfloor n/2 \rfloor \\ \sin(\lfloor n/2 \rfloor \theta) \text{ if } n \neq 2\lfloor n/2 \rfloor \end{cases} \quad n = 1, 2, \dots\,,$$

in the gPC expansion (23), which leads to the following representations of the target functional (38)

$$b_{m,n} = \int_b^a \int_0^{2\pi} g_m(\mathbf{r})\phi_n(h)\omega(r)r\mathrm{d}\theta\mathrm{d}r\,, \tag{43}$$

where the linear functional is

$$\phi_n(h) = \sum_{k=1}^{4} h(\theta, z_{\mathbf{r}}^{(k)})P_n(z_{\mathbf{r}}^{(k)})\,.$$

The weight function (39) is explicitly given by

$$\omega(r) = \sum_{k=1}^{4} \frac{1}{2\pi}\sqrt{1+\left(\frac{d\zeta}{dr}\right)^2} = \frac{\omega_{\mathrm{reg}}(r)}{\sqrt{(a-r)(r-b)}}\,, \tag{44}$$

where the regular part of (44) is given by

$$\omega_{\mathrm{reg}}(r) = \frac{2}{\pi}\sqrt{\frac{1}{r^2(a+r)(r+b)} + (a-r)(r-b)}\,.$$

4.6 Simulation: Randomly Oriented Elliptic Cylinder

In this subsection we explore numerically the randomly oriented elliptic cylinder example, that was introduced in the previous subsection. First, let us setup an inner-product preserving discretization of (43). Applying the linear change of variables on the radial variable, $r(\sigma) = \frac{a-b}{2}\sigma + \frac{a+b}{2}$, which maps (b, a) onto $(-1, 1)$, we obtain

$$\frac{1}{\sqrt{(a-r)(r-b)}} = \frac{2}{a-b}\frac{1}{\sqrt{1-\sigma^2}}\,, \quad \sigma \in (-1,1)\,.$$

Hence, we can employ the Chebyshev-Gauss quadrature in terms of σ for the integration in the radial direction,

$$r^{(i)} = \frac{a-b}{2}\sigma^{(i)} + \frac{a+b}{2}\,, \quad \sigma^{(i)} = \cos\left(\frac{2i-1}{2M}\pi\right) \quad i = 1, 2, \ldots, M\,.$$

For the angular variable we employ the composite trapezoidal rule,

$$\theta^{(i,j)} = 2\frac{j-1}{N^{(i)}}\pi \quad j = 1, 2, \ldots, N^{(i)} = 10\lfloor r^{(i)} \rfloor\,,$$

where $N^{(i)}$ is proportional to $r^{(i)}$ to accommodate for the integration over the circumference $2\pi r^{(i)}$. The corresponding spatial cubature formula is

$$\int_{\theta=0}^{2\pi}\int_{r=a}^{b} \frac{\psi(r,\theta)\ \mathrm{d}r}{\sqrt{(a-r)(r-b)}}\frac{\mathrm{d}\theta}{2\pi} \approx \sum_{i=1}^{M}\sum_{j=1}^{N^{(i)}} \psi(r^{(i)}, \theta^{(i,j)}) \cdot \frac{2\pi}{M \cdot N^{(i)}}\,.$$

Finally, using (41) and (42) we obtain the following expression for the corresponding cubature points in terms of z,

$$z^{(i,j,1)} = \theta^{(j)} - \zeta^{(i)} \quad , \quad z^{(i,j,2)} = \theta^{(j)} + \zeta^{(i)} \, ,$$
$$z^{(i,j,3)} = \theta^{(j)} - \zeta^{(i)} + \pi \, , \quad z^{(i,j,4)} = \theta^{(j)} + \zeta^{(i)} - \pi \, ,$$

where

$$\zeta^{(i)} = \arccos\left(\frac{a}{r^{(i)}} \sqrt{\frac{r^{(i)^2} - b^2}{a^2 - b^2}} \right) .$$

The resulting spatial grid $\{(r^{(i)} \cos\theta^{(i,j)}, r^{(i)} \sin\theta^{(i,j)})\}$ in $\mathcal{R}^{\rm tra}$ and the corresponding parametric grid $\{(\theta^{(i,j)}, z^{(i,j,k)})\}$ in the (θ, z)-plane are displayed in Figure (3). For comparison we show in Figure (4) a naive discretization of the random surface, whose parametric grid is uniformly distributed in the (θ, z)-plane,

$$\theta^{(j)}_{\rm naive} = 2\frac{j-1}{N}\pi \, , \; j = 1, 2, \ldots, N \, , \quad z^{(i)}_{\rm naive} = 2\frac{i-1}{M}\pi \, , \; i = 1, 2, \ldots, M \, .$$

Evidently, the corresponding naive spatial grid does a poor job in properly covering the transition region, $\mathcal{R}^{\rm tra}$.

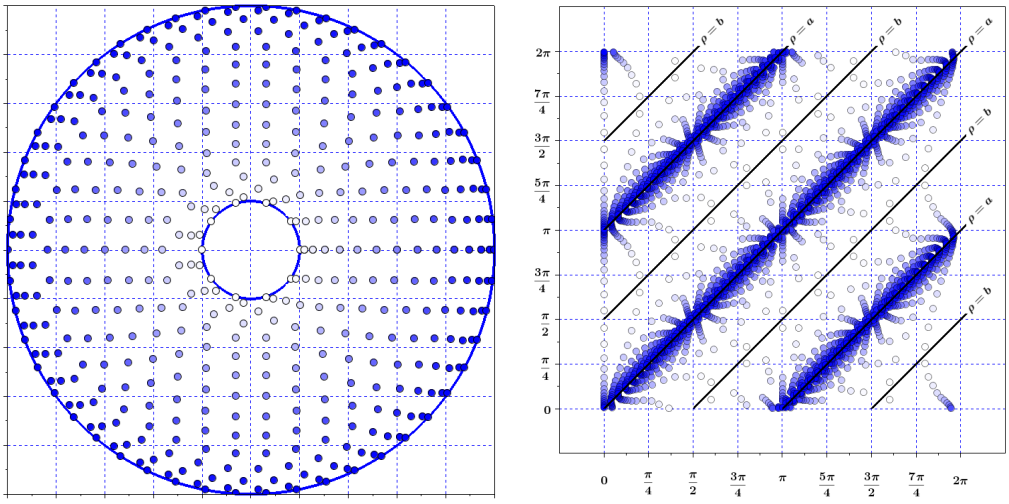

(a) the annular ($\mathcal{R}^{\rm tra}$) cubature grid. (b) the (θ, z)-plane cubature grid.

Fig. 3: **Elliptic Cylinder: Coarea discretization.** Displaying the distribution of grid points in the spatial and the parametric domains. Gridpoints intensity shifts from light at $\rho^{\min} = b$ to dark at $\rho^{\max} = a$. (a) spatial gridpoints in the annulus $\mathcal{R}^{\rm tra} \subset \mathbb{R}^2$. (b) parametric gridpoints in the (θ, z)-plane.

For the simulation we consider an elliptic cylinder whose semi-major axis is $a = 5$ and whose semi-minor axis is $b = 1$. We assume an incident plane-wave,

$$u^{\rm inc} = e^{\mathtt{i}\kappa x} = e^{\mathtt{i}\kappa r\cos\theta} = \sum_{m=-\infty}^{\infty} \mathtt{i}^m \mathrm{J}_m(\kappa r) e^{\mathtt{i}m\theta} \, , \tag{45}$$

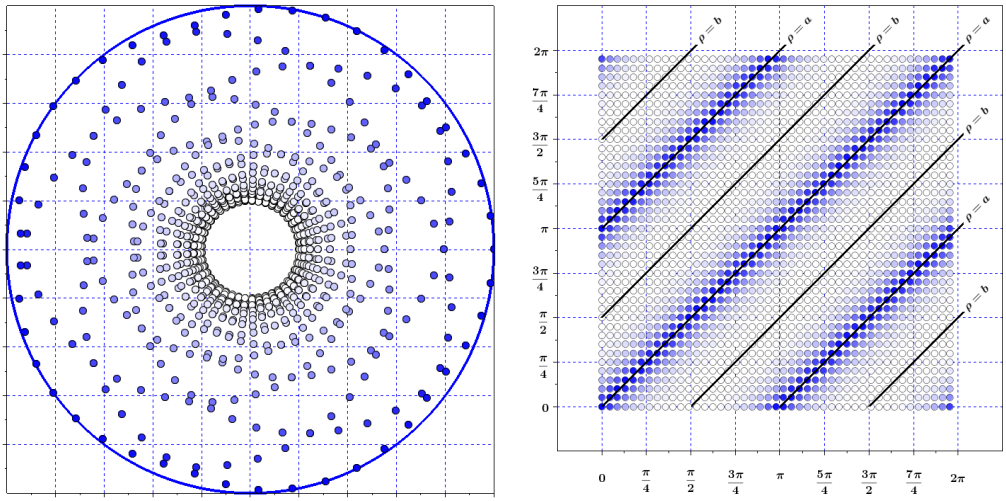

(a) the annular ($\mathcal{R}^{\mathrm{tra}}$) cubature grid. (b) the (θ, z)-plane cubature grid.

Fig. 4: **Elliptic Cylinder: Naive discretization.** Displaying the distribution of grid points in the spatial and the parametric domains. Gridpoints intesity shifts from light at $\rho^{\min} = b$ to dark at $\rho^{\max} = a$. (a) spatial gridpoints in the annulus $\mathcal{R}^{\mathrm{tra}} \subset \mathbb{R}^2$. (b) parametric gridpoints in the (θ, z)-plane.

which is approximated by truncating the infinite sum in (45) to a finite sum over the modes $|m| \leq \mu$ where μ satisfies (9). For the discretization we have used $M = 15$ and $N = 10$, and the following thresholds for the reconstruction

$$\epsilon_{\mathrm{evl}} = 10^{-4}\,, \quad \epsilon_{\mathrm{dis}} = 10^{-8}\,.$$

Figure (5) displays the construction error $\|G - \widehat{G}\|_2$, where G is a matrix whose rows are the discretized target functionals,

$$g_m(\mathbf{r}) = J_m(\kappa|\mathbf{r}|)e^{-\mathtt{i}m\theta} P_0(\mathbf{z}) = J_m(\kappa|\mathbf{r}|)e^{-\mathtt{i}m\theta}\,, \quad |m| \leq \mu\,,$$

and $\widehat{G}$ is a matrix whose rows are the corresponding reconstructed target functionals from the following set of information functionals

$$f_{\ell,m} = \mathrm{H}_m(\kappa\,|\mathbf{r} - \mathbf{r}_\ell|)e^{\mathtt{i}m\sphericalangle(\mathbf{r}-\mathbf{r}_\ell)}\,, \quad |m| \leq M\,.$$

The singular points $\mathbf{r}_\ell \in \mathcal{B}(Z)$ are uniformly distributed along the family of random surface, $\mathcal{S}(Z)$,

$$\mathbf{r}_\ell(Z) = 0.95\rho(\theta_\ell; z) \cdot (\cos\theta_\ell, \sin\theta_\ell)\,, \quad \theta_\ell = 2\frac{\ell - 1}{L}\pi\,, \quad \ell = 1, 2, \ldots, L\,.$$

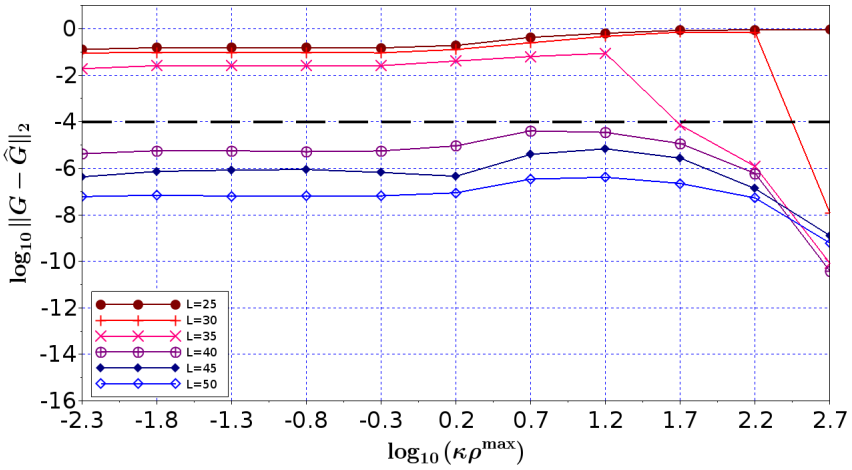

Fig. 5: **Elliptic Cylinder: Reconstruction Error.** Displaying the reconstruction error $\|G-\widehat{G}\|$ vs. $\log_{10}(\kappa)\rho^{\max}$ for various values of the parameter defining the number of target functionals, $L=25,30,\ldots,50$.

5 Randomly Shaped Polygonal Cylinders

In this section we consider the application of the theory to the general class of randomly shaped polygonal cylinders. This class is characterized by non-smooth randomly varying geometry, and thus serves a proof of concept that the proposed method can, indeed, be applied to complex shapes. The generalizations to more complex geometries is discussed in Section (6).

5.1 Piecewise Smooth Polar Form Representation

We consider a star-shape polygonal cylinder in $2D$ which is given by an ordered set of points,

$$\boldsymbol{\rho}_0=(x_0,y_0)\,,\ \ldots\,,\boldsymbol{\rho}_{Q-1}=(x_{Q-1},y_{Q-1})\,,\boldsymbol{\rho}_Q=\boldsymbol{\rho}_0\,,$$

counter-clockwise distributed in $\mathbb{R}^2$,

$$0\le\theta_{q-1}=\arctan(y_{q-1}/x_{q-1})<\arctan(y_q/x_q)=\theta_q\le 2\pi\,, \tag{46}$$

that describe the boundary of the polygon where $\mathcal{S}_q$ is the line connecting $\boldsymbol{\rho}_{q-1}$ and $\boldsymbol{\rho}_q$,

$$\mathcal{S}=\bigcup_{\ell=1}^{Q}\mathcal{S}_q\,,\quad \mathcal{S}_q=\left\{\,\boldsymbol{\rho}_{q-1}+t(\boldsymbol{\rho}_q-\boldsymbol{\rho}_{q-1})\middle|\ t\in[0,1]\right\}\,,$$

for all $q=1,2,\ldots,Q$. We also assume that the points $\boldsymbol{\rho}_q$ are smooth functions of a random vector $\mathbf{Z}\in\mathcal{I}_{\mathbf{Z}}$, defining simple open differentiable curves that do not intersect in $2D$ space. In particular each curve does not cross itself.

For a polar representation we consider an arbitrary $\mathcal{S}_q$. The equality

$$(\xi,\psi)=\boldsymbol{\rho}=\boldsymbol{\rho}_{q-1}+t(\boldsymbol{\rho}_q-\boldsymbol{\rho}_{q-1})\,,$$

is equivalent to the system

$$\begin{aligned}\xi(\mathbf{z},t)&=\rho\cos\theta=x_{q-1}+t\cdot(x_q-x_{q-1})\,,\\ \psi(\mathbf{z},t)&=\rho\sin\theta=y_{q-1}+t\cdot(y_q-y_{q-1})\ .\end{aligned}$$

where for every $\mathbf{z}\in\mathcal{I}_{\mathbf{Z}}$, $\theta(\mathbf{z},t)\in[\theta_{q-1},\theta_q]$. Assuming $t=t(\theta;\mathbf{z})\in[0,1]$, we obtain

$$t(\theta;\mathbf{z})=\frac{x_{q-1}\sin\theta-y_{q-1}\cos\theta}{(y_q-y_{q-1})\cos\theta-(x_q-x_{q-1})\sin\theta}=\frac{\rho(\theta;\mathbf{z})}{\rho_q(\mathbf{z})}\cdot\frac{\sin(\theta-\theta_{q-1})}{\sin(\theta_q-\theta_{q-1})}\,,$$

which leads to the following expressions

$$\rho(\theta;\mathbf{z})=\frac{\rho_q\rho_{q-1}\sin(\theta_q-\theta_{q-1})}{\rho_q\sin(\theta_q-\theta)+\rho_{q-1}\sin(\theta-\theta_{q-1})}\,, \tag{47}$$

$$\frac{\partial\rho}{\partial\theta}(\theta;\mathbf{z})=\rho(\theta;\mathbf{z})\cdot\frac{\rho_q\cos(\theta_q-\theta)-\rho_{q-1}\cos(\theta-\theta_{q-1})}{\rho_q\sin(\theta_q-\theta)+\rho_{q-1}\sin(\theta-\theta_{q-1})}\,, \tag{48}$$

where $\rho_q(\mathbf{z})=\sqrt{x_q^2+y_q^2}$.

5.2 Considerations for Setting the Spatial Cubature for a Single random Variable

Let $\mathbf{Z}=Z\in[-1,1]$ with a given probability density function $\frac{dF(z)}{dz}$, and consider the functional (38) represented as sum of integrals on the sides of the polygon,

$$\begin{aligned}b_{m,n}&=\sum_{q=1}^{Q}\iint_{\mathcal{R}_q}g_m(\mathbf{r})\left[\sum_{z_{\mathbf{r}}\in\mathcal{I}_{Z_{\mathbf{r}}},\mathbf{r}\in\mathcal{R}_q}h(\theta;z_{\mathbf{r}})P_n(z_{\mathbf{r}})\,|\nabla z_{\mathbf{r}}|\,\frac{dF_Z}{dz}(z_{\mathbf{r}})\right]r\,\mathrm{d}\theta\,\mathrm{d}r\,,\\ &=\sum_{q=1}^{Q}\iint_{\mathcal{R}_q}g_m(\mathbf{r})\phi_n^{(q)}(h)\omega^{(q)}(\mathbf{r})r\,\mathrm{d}\theta\,\mathrm{d}r\,,\end{aligned} \tag{49}$$

where the subdomains of integration are

$$\mathcal{R}_q=\left\{\mathbf{r}\in\mathcal{R}^{\mathrm{tra}}\,\middle|\,\exists z\in\mathcal{I}_Z\ :\ \mathbf{r}\in\mathcal{S}_q(z)\right\}\subset\mathbb{R}^2\,. \tag{50}$$

The corresponding weight functions are

$$\omega^{(q)}(\mathbf{r})=\sum_{z_{\mathbf{r}}\in\mathcal{I}_{Z_{\mathbf{r}}}}|\nabla z_{\mathbf{r}}|\frac{dF_Z}{dz}(z_{\mathbf{r}})\,,\quad\mathbf{r}\in\mathcal{R}_q\,,$$

and the bounded linear functional (40) is given by

$$\phi_n^{(q)}(h)=\sum_{z_{\mathbf{r}}\in\mathcal{I}_{Z_{\mathbf{r}}}}h(\theta;z_{\mathbf{r}})P_n(z_{\mathbf{r}})\left[\sum_{y_{\mathbf{r}}\in\mathcal{I}_{Z_{\mathbf{r}}}\setminus\{z_{\mathbf{r}}\}}|\nabla y_{\mathbf{r}}|\frac{dF_Z}{dz}(y_{\mathbf{r}})\right]^{-1}\,,\quad\mathbf{r}\in\mathcal{R}_q\,.$$

Note, that by our definitions for any $q\neq q'$, $\mathcal{R}_q\cap\mathcal{R}_{q'}$ is a zero measure Jordan set and $\cup_q\mathcal{R}_q$ is a subset of $\mathcal{R}^{\mathrm{tra}}$ but not equal to $\mathcal{R}^{\mathrm{tra}}$ (22).

To define a proper cubature rule we must identify the zeros of $\partial_z \rho(\theta; z)$ and their local behavior, i.e., *Taylor expansion*. Note, that (37) implies that when $|\partial_\theta z_{\mathbf{r}}|$ exists (i.e., a finite and real) then any zero of $\partial_z \rho(\theta; z)$ is also a zero of $\partial_\theta \rho(\theta; z)$, which is easier to compute. Indeed, by (48) it is sufficient to solve the equalities

$$\rho_q \cos(\theta_q - \theta) = \rho_{q-1} \cos(\theta - \theta_{q-1}) \,, \quad q = 1, 2, \ldots, Q \,.$$

Finally, we note that, in general, $\rho(\theta; z)$ as well as $\partial_z \rho(\theta; z)$ are not smooth as functions of θ across the angels $\theta_q(z)$ (46). Thus, we must construct a separate cubature rule for each integral associated with each sub-domain $\mathcal{R}_q$ in (49).

5.3 Numerical Example

Consider a star shaped octagonal cylinder whose vertices are given in Table (1), where $a > b > a/2 > 0$ and the random variable Z is uniformly distributed in $[-1, 1]$. When $z = -1$ the shape is non-convex star polygon. As z increases the shape eventually becomes convex and gradually transforms to a full square at $z = 1$. See Figure (6) for an illustration. Note, that the radial bounds are

$$\rho^{\min} = \sqrt{2}(a - b) < \sqrt{2}(a + b) = \rho^{\max} \,.$$

q	$\boldsymbol{\rho}_{q-1} = (x_{q-1}, y_{q-1})$	$\boldsymbol{\rho}_q = (x_q, y_q)$	$[\theta_{q-1}, \theta_q]$
1	$(a + b(z+1)/2, 0)$	$(a + bz, a + bz)$	$[0, \pi/4]$
2	$(a + bz, a + bz)$	$(0, a + b(z+1)/2)$	$[\pi/4, \pi/2]$
3	$(0, a + b(z+1)/2)$	$(-a - bz, a + bz)$	$[\pi/2, 3\pi/4]$
4	$(-a - bz, a + bz)$	$(-a - b(z+1)/2, 0)$	$[3\pi/4, \pi]$
5	$(-a - b(z+1)/2, 0)$	$(-a - bz, -a - bz)$	$[\pi, 5\pi/4]$
6	$(-a - bz, -a - bz)$	$(0, -a - b(z+1)/2)$	$[5\pi/4, 3\pi/2]$
7	$(0, -a - b(z+1)/2)$	$(a + bz, -a - bz)$	$[3\pi/2, 7\pi/4]$
8	$(a + bz, -a - bz)$	$(a + b(z+1)/2, 0)$	$[7\pi/4, 2\pi]$

Table 1: **Star Shaped Octagonal Cylinder Polar Form Parameters.**

The data in Table (6), in fact, satisfies the following formula

$$\theta_q = q\frac{\pi}{4} \,, \quad \rho_q = \frac{1 + (-1)^q}{2} \left(a + \frac{b}{2}(z+1) \right) + \frac{1 - (-1)^q}{2} \sqrt{2}(a + bz) \,,$$

where $q \in \{1, 2, \ldots, 8\}$ denotes the index of the segment. Using (47) we have

$$\rho(\theta; z) = \frac{(a + bz) \cdot \left(a + \frac{b}{2} + \frac{b}{2} z \right)}{\sqrt{2}(a + bz) \cdot \alpha_q(\theta) + \left(a + \frac{b}{2} + \frac{b}{2} z \right) \cdot \beta_q(\theta)} \,,$$

where

$$\alpha_q = \frac{1 + (-1)^q}{2} \sin\left(\theta - q\frac{\pi}{4} + \frac{\pi}{4} \right) + \frac{1 - (-1)^q}{2} \sin\left(q\frac{\pi}{4} - \theta \right) \,,$$
$$\beta_q = \frac{1 + (-1)^q}{2} \sin\left(q\frac{\pi}{4} - \theta \right) + \frac{1 - (-1)^q}{2} \sin\left(\theta - q\frac{\pi}{4} + \frac{\pi}{4} \right) \,.$$

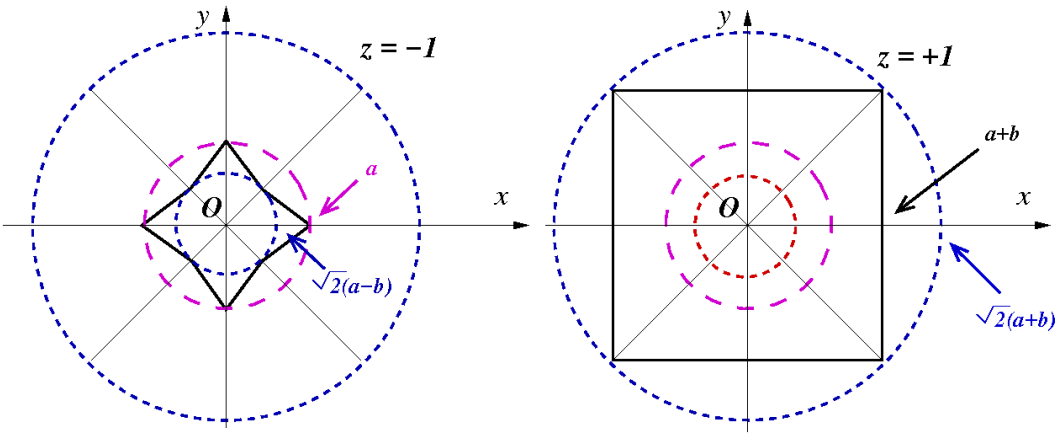

Fig. 6: **Polygonal Cylinder: random shape at $z = \pm 1$.**

By direct calculations we obtain

$$\frac{\partial \rho}{\partial z}(\theta; z) = b\rho^2(\theta; z) \cdot \left(\frac{\beta_q(\theta)}{a + bz} + \frac{\alpha_q(\theta)}{2a + b + bz} \right),$$

which is strictly positive for all $\theta \in (\theta_{q-1}, \theta_q)$ and any $q = 1, 2, \ldots, 8$. Hence, $\partial_z \rho \neq 0$ for all $(z, \theta) \in [-1, 1] \times [0, 2\pi]$.

We observe that in the current example each sub-domain of integration $\mathcal{R}_q$ (50) is a quadrilateral in $\mathbb{R}^2$ whose corners are given by $\rho(\theta_{q-1}, \pm 1) \cdot (\cos\theta_{q-1}, \sin\theta_{q-1})$, and $\rho(\theta_q, \pm 1) \cdot (\cos\theta_q, \sin\theta_q)$, as illustrated in Figure (7). Hence, we setup the

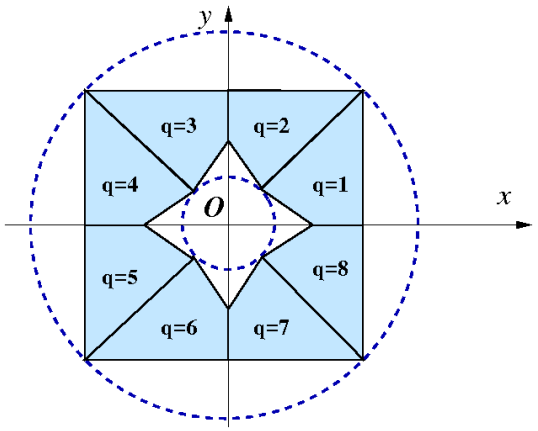

Fig. 7: **Polygonal Cylinder: sub-domains of integration, $\mathcal{R}_q$.**

cubature rule by mapping each quadrilateral $\mathcal{R}_q$ onto $[-1, 1] \times [-1, 1]$ followed by applying Gauss-Legendre quadratures. The explicit implementation is as follows:

1. Linearly map the angular segment $[\theta_{q-1}, \theta_q]$ onto $[-1, 1]$,
$$\theta(\tau) = \frac{\pi}{8}(\tau + 2q - 1)\,, \quad \tau \in [-1, 1]\,.$$
2. Evaluate the $N_q \in \mathbb{N}$ Gauss-Legendre quadrature nodes in τ,
$$-1 < \tau^{(q,1)} < \tau^{(q,2)} < \cdots < \tau^{(q,N_q)} < 1\,.$$
3. For each $\theta^{(q,j)} = \theta(\tau^{(q,j)})$ apply linear map in the radial direction
$$r^{(q,j)}(\sigma) = \frac{\rho(\theta^{(q,j)}; 1) - \rho(\theta^{(q,j)}; -1)}{2} \cdot \sigma + \frac{\rho(\theta^{(q,j)}; 1) + \rho(\theta^{(q,j)}; -1)}{2}\,.$$
4. Evaluate the $M_q \in \mathbb{N}$ Gauss-Legendre quadrature nodes in σ,
$$-1 < \sigma^{(q,1)} < \sigma^{(q,2)} < \cdots < \sigma^{(q,M_q)} < 1\,.$$

The overall discretized approximation of (49) becomes

$$\sum_{q=1}^{8} \sum_{i=1}^{M_q} \sum_{j=1}^{N_q} \left[h(\mathbf{r}, z_{\mathbf{r}})\, |\partial_r z_{\mathbf{r}}|\right]_{\mathbf{r}=\mathbf{r}^{(q,i,j)}} P_n(z_{\mathbf{r}^{(q,i,j)}}) r^{(q,i,j)} \omega^{(q,i,j)}\,,$$

where

$$\begin{aligned}
r^{(q,i,j)} &= \frac{\rho(\theta^{(q,j)}; 1) - \rho(\theta^{(q,j)}; -1)}{2} \cdot \sigma^{(q,i)} + \frac{\rho(\theta^{(q,j)}; 1) + \rho(\theta^{(q,j)}; -1)}{2}\,,\\
\mathbf{r}^{(q,i,j)} &= (r^{(q,i,j)} \cos\theta^{(q,j)}, r^{(q,i,j)} \sin\theta^{(q,j)})\,,\\
\omega^{(q,i,j)} &= \frac{\pi}{4} \cdot \frac{\rho(\theta^{(q,j)}; 1) - \rho(\theta^{(q,j)}; -1)}{\left[(1-s^2)P'_{N_q}(\sigma)\right]_{\sigma=\sigma^{(q,i)}} \cdot \left[(1-\tau^2)P'_{M_q}(\tau)\right]_{\tau=\tau^{(q,j)}}}\,.
\end{aligned}$$

An illustration of the spatial integration nodes admitted by the procedure suggested above is given in Figure (8).

For the simulation we consider the star-shaped polygonal as given in Table (6), whose parameters are $a = 5$ and $b = 4$. We assume an incident plane-wave,

$$u^{\text{inc}} = e^{\mathtt{i}\kappa x} = e^{\mathtt{i}\kappa r\cos\theta} = \sum_{m=-\infty}^{\infty} \mathtt{i}^m \mathrm{J}_m(\kappa r) e^{\mathtt{i}m\theta}\,, \tag{51}$$

which is approximated by truncating the infinite sum in (51) to a finite sum over the modes $|m| \le \mu$ where μ satisfies (9). For the discretization we have used $M_q \equiv 15$ and $N_q \equiv 12$, and the thresholds $\epsilon_{\text{evl}} = 10^{-4}$ and $\epsilon_{\text{dis}} = 10^{-8}$ for the reconstruction. Figure (9) displays the construction error $\|G - \widehat{G}\|_2$, where G is a matrix whose rows are the discretized target functionals,

$$g_m(\mathbf{r}) = J_m(\kappa|\mathbf{r}|)e^{-\mathtt{i}m\theta} P_0(\mathbf{z}) = J_m(\kappa|\mathbf{r}|)e^{-\mathtt{i}m\theta}\,, \quad |m| \le \mu\,,$$

and $\widehat{G}$ is a matrix whose rows are the corresponding reconstructed target functionals. For the reconstruction We employed the following information functionals

$$f_{\ell,m} = \mathrm{H}_m(\kappa\,|\mathbf{r} - \mathbf{r}_\ell|)e^{\mathtt{i}m\sphericalangle(\mathbf{r}-\mathbf{r}_\ell)}\,, \quad |m| \le M_q$$

whose singularities $\mathbf{r}_\ell = 0.95\rho(\theta_\ell; z) \cdot (\cos\theta_\ell, \sin\theta_\ell) \in \mathcal{B}(Z)$ are uniformly distributed along the family of random surface, $\mathcal{S}(Z)$; $\theta_\ell = 2\frac{\ell-1}{L}\pi$, $\ell = 1, 2, \ldots, L$.

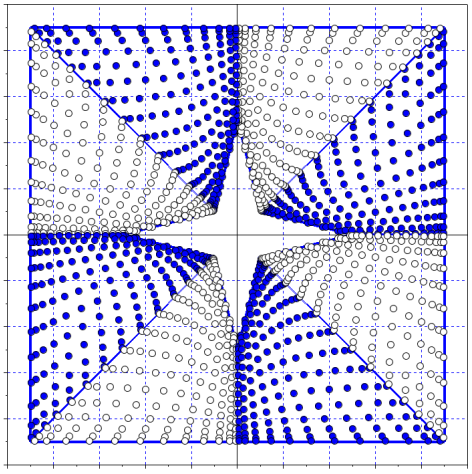

Fig. 8: **Polygonal Cylinder: Coarea discretization.** Gridpoints intensity interchages between light or dark in adjacent subdomains $\mathcal{R}_q \quad (q = 1, \ldots, 8)$.

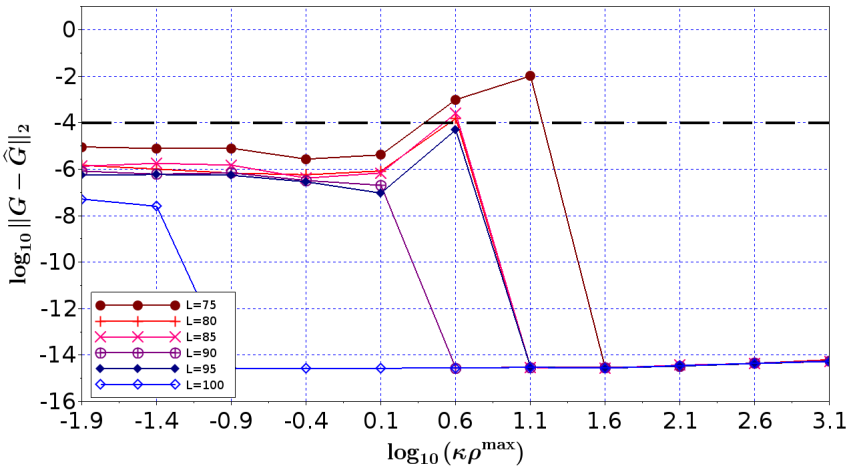

Fig. 9: **Polygonal Cylinder: Reconstruction Error.** Displaying the reconstruction error $\|G - \widehat{G}\|$ vs. $\log_{10}(\kappa\rho^{\max})$ for varous numbers of the parameter defining the number of target functionals, $L = 75, 80, \ldots, 100$.

6 Summary and Future Study

The present paper introduced an alternative approach for quantifying the effects of random shape in acoustic scattering problems. The core idea of the proposed method is to construct a spatial embedding within the family of random surfaces which facilitates a natural choice of a spatial low-dimensional integration rule. The chosen integration weight function is positive, encompasses random surface irregularities and of minimal variance. This essentially avoids the fundamental

problems associated with random surface discretizations, namely lack of smoothness in the proximity of the surface when using a level-set method and strong non-linear dependence on the variation of the boundary when utilizing random domain mapping. The efficacy of the proposed approach was demonstrated on model problems in $\mathbb{R}^2$.

Generalizing the new approach to non star-shaped obstacles as well as to $3D$ spatial setting is straightforward. Indeed, given a non star-shaped obstacle we can represent its random boundary as a union of star-shaped sub-surfaces each with a local origin. For a star-shaped obstacle in $\mathbb{R}^3$ the surface of the obstacle possesses a spherical representation,

$$\mathcal{S}^{3D}(\mathbf{Z}) = \{\, (\rho\cos\theta\cos\varphi, \rho\cos\theta\sin\varphi, \rho\sin\theta) |\ \theta \in [0,\pi]\,,\ \varphi\in[0,2\pi]\} \ ,$$

where $\rho = \rho(\theta,\varphi;\mathbf{Z})$. Thus, the gPC expansion of the scattering coefficients (8) can be represented by

$$b^m_{n,\mathbf{n}} = \int\limits_{\mathbf{z}\in\mathcal{I}_{\mathbf{Z}}} \cdots \int \left[\int\limits_{\theta=0}^{\pi} \int\limits_{\varphi=0}^{2\pi} h(\boldsymbol{\rho})\cdot g^m_n(\boldsymbol{\rho}) P_{\mathbf{n}}(\mathbf{z}) S(\theta,\varphi;\mathbf{z})\,\mathrm{d}\theta\,\mathrm{d}\varphi \right] \prod_{p=1}^{P} \mathrm{d}F_{Z_p}\,,$$

where $g^m_n(\mathbf{r}) = -\mathrm{j}_n(\kappa\mathbf{r})P_n^{|m|}(\cos\varphi)e^{\mathrm{i}m\theta}$, $\boldsymbol{\rho}(\theta,\varphi;\mathbf{z}) = (\rho\cos\theta\cos\varphi, \rho\cos\theta\sin\varphi, \rho\sin\theta)$ and the metric tensor for the spherical case is given by

$$S(\theta,\varphi;\mathbf{Z}) = \rho\sqrt{\left(\rho^2 + \left(\frac{\partial\rho}{\partial\varphi}\right)^2\right)\sin^2\varphi + \left(\frac{\partial\rho}{\partial\theta}\right)^2} \qquad (\rho = \rho(\theta,\varphi;\mathbf{z}))\ .$$

Employing the Coarea formula with respect to the level sets of $\boldsymbol{\Phi}(\mathbf{z},\theta,\varphi) = \boldsymbol{\rho}(\theta,\varphi;\mathbf{z})$ yields an expression similar to (28)

$$b^m_{n,\mathbf{n}} = \iiint\limits_{\mathcal{R}^{\mathrm{tra}}} g^m_n(\mathbf{r})\phi_{\mathbf{n}}(h)\omega(\mathbf{r})r^2\sin\theta\,\mathrm{d}\theta\,\mathrm{d}r\,,$$

where the $3D$ transition region is

$$\mathcal{R}^{\mathrm{tra}} = \left\{ \mathbf{r}\in\mathbb{R}^3 \,\middle|\, \inf_{\theta,\varphi,\mathbf{z}} \rho(\theta,\varphi;\mathbf{z}) < |\mathbf{r}| < \sup_{\theta,\varphi,\mathbf{z}} \rho(\theta,\varphi;\mathbf{z}) \right\} \subset \mathbb{R}^3\,,$$

and the weight function is proportional to the conditional expectetation of the normalized metric tensor,

$$\omega(\mathbf{r}) = \mathbb{E}\left[\frac{S(\theta,\varphi;\mathbf{z})}{\rho^2\sin\theta} \,\middle|\, \rho(\theta,\varphi;\mathbf{z}) = r \right] \cdot f_\rho(\mathbf{z})\,.$$

The expressions are, however, technically more complicated to work with. The usage of automatic integration as well as optimization methods for obtaining the spatial grid may prove to be a necessity.

Another challenge is to efficiently deal with several random variables. This can be achieved by employing the single random variable formula (35) as a basic building block. Indeed, in the $2D$ case, choosing a single random variable, Z_p, and

applying the coarea formula (28) with respect to the corresponding integration variable z_p yields the following equivalent representation

$$b_{m,\mathbf{n}} = \iint\limits_{\mathcal{R}^{\mathrm{tra}}} g_m(\mathbf{r})\phi_{\mathbf{n}}(h)\omega(\mathbf{r})r\,\mathrm{d}\theta\,\mathrm{d}r\,,$$

where the functional operating on h explicitly satisfies

$$\phi_{\mathbf{n}}(h)\omega(\mathbf{r}) = \int\limits_{\mathcal{I}_{\mathbf{Z}}\setminus\mathcal{I}_{Z_p}}\cdots\int\left[\sum_{z_{p,\mathbf{r}}\in\mathcal{I}_{Z_{p,\mathbf{r}}}} h(\mathbf{z},\theta)P_{\mathbf{n}}(\mathbf{z})\frac{s(\theta;z)}{\left|\partial_{z_p}\rho\right|_{z_p=z_{p,\mathbf{r}}}}\frac{dF_{Z_p}}{dz_p}(z_{p,\mathbf{r}})\right]\prod_{q\neq p}\mathrm{d}F_{Z_q}\,,$$

and the zero dimensional fiber set corresponding to Z_p is

$$\mathcal{I}_{Z_{p,\mathbf{r}}} = \left\{\, z\in\mathcal{I}_{Z_p}\,\middle|\,\boldsymbol{\rho}(\theta;\mathbf{z}) = \mathbf{r}\right\}\subset\mathcal{I}_{Z_p}\,.$$

Note that $z_{p,\mathbf{r}}$ is a function of $\mathbf{r}$ as well as $z_1,\ldots,z_{p-1},z_{p+1},\ldots,z_P$. In general, globally using the last formula is not expected to produce an optimal result. A more sophisticated approach is to partition $\mathcal{R}^{\mathrm{tra}}$ into subregions where each subregion is associated with one significant random variable. This, requires performing sensitivity analysis, similar to the *analysis of variance* (ANOVA) method [15], that is also dependent on the spatial coordinates, $\mathbf{r}$. The exploration of this approach needs a separate extensive study, and deferred to future work.

References

1. A. Ditkowski, Y.H.: Wave scattering by randomly shaped objects. J. Applied Numerical Mathematics **62**, 1819–1836 (2012)
2. Bejan, A.: Shape and Structure, from Engineering to Nature. Shape and Structure, from Engineering to Nature. Cambridge University Press (2000)
3. Canuto, C., Kozubek, T.: A fictitious domain approach to the numerical solutions of PDEs in stochastic domains. Numer. Math. **107**, 257–293 (2007)
4. Castrillón-Candás, J.E., Nobile, F., Tempone, R.F.: Analytic regularity and collocation approximation for elliptic pdes with random domain deformations. Computers & Mathematics with Applications **71**(6), 1173 – 1197 (2016)
5. Colton, D., Kress, R.: Inverse Acoustic and Electromagnetic Scattering Theory, Second Edition. Springer (1998)
6. Davis, P.J., Rabinowitz, P.: Methods of numerical integration. Courier Dover Publications (2007)
7. Dini, U.: Lezioni di analisi infinitesimale. Universitá di Pisa, Pisa, Italy (1887)
8. Federer, H.: Curvature measures. Transactions of the American Mathematical Society **93**(3), 418–491 (1959)
9. Ghanem, R.G., Spanos, P.: Stochastic Finite Elements: A Spectral Approach. Springer Verlag (2002)
10. Golomb, M., Weinberger, H.F.: Optimal approximation and error bounds in Numerical Approximation. University of Wisconsin Press, Wisconsin Madison (1959)
11. Harbrecht, H., Peters, M., Siebenmorgen, M.: Analysis of the domain mapping method for elliptic diffusion problems on random domains. Numerische Mathematik **134**(4), 823–856 (2016)
12. Harness, Y.: Wave Scattering by Randomly Shaped Obstacles. Thesis, Tel Aviv University (2013)
13. Harness, Y., Ditkowski, A.: The null-field method: a reconstruction kernel approach. J. Comput. Phys. **248**, 127–146 (2013)
14. Hiptmair, R., Scarabosio, L., Schillings, C., Schwab, C.: Large deformation shape uncertainty quantification in acoustic scattering. Tech. rep., Zürich (2015)

15. Holtz, M.: Sparse Grid Quadrature in High Dimensions with Applications in Finance and Insurance. Lecture Notes in Computational Science and Engineering. Springer Berlin Heidelberg (2010)
16. Kress, R.: Linear Integral Equations. Applied Mathematical Sciences. Springer New York (2013)
17. Louis, A.K.: Feature reconstruction in inverse problems. Inverse Problems **27**(6)
18. Louis, A.K.: A unified approach to regularization methods for linear ill-posed problems. Inverse Problems **15**, 489–498 (1999)
19. Louis, A.K., Maass, P.: A mollifier method for linear operator equations of the first kind. Inverse Problems **6**, 427–440 (1990)
20. Martin, P.: Multiple Scattering: Interaction of Time-Harmonic Waves with N Obstacles. Cambridge University Press (2006)
21. Micchelli, C.A., Rivlin, T.J.: A survey of optimal recovery in Optimal Estimation in Approximation Theory. Plenum Press, New York (1985)
22. Nouy, A., Clment, A., Schoefs, F., Moës, N.: An extended stochastic finite element method for solving stochastic partial differential equations on random domains. Computer Methods in Applied Mechanics and Engineering **197**(51-52), 4663 – 4682 (2008)
23. Nouy, A., Schoefs, F., Moës, N.: X-sfem, a computational technique based on x-fem to deal with random shapes. European Journal of Computational Mechanics **16**(2), 277–293 (2007)
24. Sauter, S., Schwab, C.: Boundary Element Methods. Springer Series in Computational Mathematics. Springer Berlin Heidelberg (2010)
25. Sethian, J.: Level Set Methods and Fast Marching Methods: Evolving Interfaces in Computational Geometry, Fluid Mechanics, Computer Vision, and Materials Science. Cambridge Monographs on Applied and Computational Mathematics. Cambridge University Press (1999)
26. Tartakovsky, D., Xiu, D.: Numerical methods for differential equations in random domain. SIAM J. Sci. Comput. **28**(3), 1167–1185 (2006)
27. Tartakovsky, D., Xiu, D.: Stochastic analysis of transport in tubes with rough walls. J. Comput. Phys. **217**(1), 248–259 (2006)
28. Wan, X., Xiu, D., Karnidakis, G.E.: Modeling uncertainty in flow simulations via generalized polynomial chaos. J. Comput. Phys. **187**, 137–167 (2003)
29. Warnick, K., Chew, W.: Numerical simulation methods for rough surface scattering. Waves in Random & Complex Media **11**(1), 1–30 (2001)
30. Waterman, P.C.: Matrix formulation of electromagnetic scattering. Proceedings of the IEEE **53**(8), 805–812 (1965)
31. Waterman, P.C.: New formulation of acoustic scattering. J. Acoust. Soc. Am. **45**(6), 1417–1429 (1969)
32. Wiener, N.: The homogeneous chaos. Amer. J. Math. **60**, 897–936 (1938)
33. Wriedt, T.: Light scattering theory and programs: discussion of latest advances and open problems. Journal of Quantitative Spectroscopy and Radiative Transfer **113**, 2465–2469 (2012)
34. Xiu, D.: Numerical Methods for Stochastic Computations: A Spectral Method Approach. Princeton University Press (2010)
35. Xiu, D., Karnidakis, G.E.: Modeling uncertainty in steady state diffusion problems via generalized polynomial chaos. Comput. Methods Appl. Math. Eng. **11**, 4927–4948 (2002)
36. Xiu, D., Karnidakis, G.E.: The wiener-askey polynomial chaos for stochastic differential equations. SIAM J. Sci. Comput. **24**(2), 26–40 (2002)